



NAVAL POSTGRADUATE SCHOOL

MONTEREY, CALIFORNIA

THESIS

**HYDRODYNAMIC DRAG FORCE MEASUREMENT OF
A FUNCTIONALIZED SURFACE EXHIBITING
SUPERHYDROPHOBIC PROPERTIES**

by

James R. Ley

December 2016

Thesis Advisor:
Second Reader:

Young W. Kwon
Jarema M. Didoszak

Approved for public release. Distribution is unlimited.

THIS PAGE INTENTIONALLY LEFT BLANK

REPORT DOCUMENTATION PAGE			<i>Form Approved OMB No. 0704-0188</i>	
Public reporting burden for this collection of information is estimated to average 1 hour per response, including the time for reviewing instruction, searching existing data sources, gathering and maintaining the data needed, and completing and reviewing the collection of information. Send comments regarding this burden estimate or any other aspect of this collection of information, including suggestions for reducing this burden, to Washington headquarters Services, Directorate for Information Operations and Reports, 1215 Jefferson Davis Highway, Suite 1204, Arlington, VA 22202-4302, and to the Office of Management and Budget, Paperwork Reduction Project (0704-0188) Washington, DC 20503.				
1. AGENCY USE ONLY (Leave blank)		2. REPORT DATE December 2016		3. REPORT TYPE AND DATES COVERED Master's thesis
4. TITLE AND SUBTITLE HYDRODYNAMIC DRAG FORCE MEASUREMENT OF A FUNCTIONALIZED SURFACE EXHIBITING SUPERHYDROPHOBIC PROPERTIES			5. FUNDING NUMBERS	
6. AUTHOR(S) James R. Ley				
7. PERFORMING ORGANIZATION NAME(S) AND ADDRESS(ES) Naval Postgraduate School Monterey, CA 93943-5000			8. PERFORMING ORGANIZATION REPORT NUMBER	
9. SPONSORING /MONITORING AGENCY NAME(S) AND ADDRESS(ES) N/A			10. SPONSORING / MONITORING AGENCY REPORT NUMBER	
11. SUPPLEMENTARY NOTES The views expressed in this thesis are those of the author and do not reflect the official policy or position of the Department of Defense or the U.S. Government. IRB number ____N/A____.				
12a. DISTRIBUTION / AVAILABILITY STATEMENT Approved for public release. Distribution is unlimited.			12b. DISTRIBUTION CODE	
13. ABSTRACT (maximum 200 words) <p>With superhydrophobic properties being extended to a variety of metallic substrates through the process of ablation due to femto-second laser surface processing (FLSP), it is important to understand the hydrodynamic benefits of such a material, as well as its resiliency. This research will focus on the skin friction drag effects of a superhydrophobic flat plate compared to an untreated flat plate of the same material and geometry. The resiliency of this material will also be tested through the use of an accelerated corrosion fog chamber using both treated and untreated aluminum samples.</p> <p>During complete submersion water channel testing, the velocity of the water was varied to yield a range of Reynolds numbers between 20,000 and 70,000 with respect to the test specimen. In this range, the FLSP treated plate showed consistently lower skin friction drag than that of the untreated plate. However, during the accelerated corrosion testing, the FLSP treated sample suffered from pitting corrosion at a rate faster than the untreated sample, effectively removing the surface treatment. While there are significant hydrodynamic benefits to this material, the elevated corrosion rates raise concerns about the resiliency of this surface treatment.</p>				
14. SUBJECT TERMS superhydrophobic, superhydrophilic, Femto-second laser surface processing, skin friction drag			15. NUMBER OF PAGES 77	
			16. PRICE CODE	
17. SECURITY CLASSIFICATION OF REPORT Unclassified		18. SECURITY CLASSIFICATION OF THIS PAGE Unclassified		19. SECURITY CLASSIFICATION OF ABSTRACT Unclassified
20. LIMITATION OF ABSTRACT UU				

THIS PAGE INTENTIONALLY LEFT BLANK

Approved for public release. Distribution is unlimited.

**HYDRODYNAMIC DRAG FORCE MEASUREMENT OF A FUNCTIONALIZED
SURFACE EXHIBITING SUPERHYDROPHOBIC PROPERTIES**

James R. Ley
Lieutenant, United States Navy
B.S., Purdue University, 2009

Submitted in partial fulfillment of the
requirements for the degree of

MASTER OF SCIENCE IN MECHANICAL ENGINEERING

from the

**NAVAL POSTGRADUATE SCHOOL
December 2016**

Approved by: Young W. Kwon
Thesis Advisor

Jarema M. Didoszak
Second Reader

Garth V. Hobson
Chair, Department of Mechanical and Aerospace Engineering

THIS PAGE INTENTIONALLY LEFT BLANK

ABSTRACT

With superhydrophobic properties being extended to a variety of metallic substrates through the process of ablation due to femto-second laser surface processing (FLSP), it is important to understand the hydrodynamic benefits of such a material, as well as its resiliency. This research will focus on the skin friction drag effects of a superhydrophobic flat plate compared to an untreated flat plate of the same material and geometry. The resiliency of this material will also be tested through the use of an accelerated corrosion fog chamber using both treated and untreated aluminum samples.

During complete submersion water channel testing, the velocity of the water was varied to yield a range of Reynolds numbers between 20,000 and 70,000 with respect to the test specimen. In this range, the FLSP treated plate showed consistently lower skin friction drag than that of the untreated plate. However, during the accelerated corrosion testing, the FLSP treated sample suffered from pitting corrosion at a rate faster than the untreated sample, effectively removing the surface treatment. While there are significant hydrodynamic benefits to this material, the elevated corrosion rates raise concerns about the resiliency of this surface treatment.

THIS PAGE INTENTIONALLY LEFT BLANK

TABLE OF CONTENTS

I.	INTRODUCTION.....	1
A.	BACKGROUND	1
B.	PRIOR RESEARCH	3
C.	RECENT DEVELOPMENTS	6
D.	OBJECTIVE	8
II.	FABRICATION AND EXPERIMENTAL METHODS	9
A.	WATER TUNNEL DESIGN AND FABRICATION	9
1.	Channel Design.....	9
2.	Removable Top Design	13
3.	Receiving Fixture Design.....	14
B.	SPECIMEN FIXTURE DESIGN AND FABRICATION	15
1.	Initial Concept.....	16
2.	Final Design	18
C.	SENSOR DESIGN, FABRICATION, AND INTEGRATION	18
1.	Initial Concept.....	19
2.	Final Design	19
a.	<i>Preliminary Concept Design.....</i>	<i>19</i>
b.	<i>Practical Application Design</i>	<i>21</i>
D.	WATER CHANNEL TEST STAND AND ANCILLARY EQUIPMENT.....	23
1.	Test Stand	23
2.	Ancillary Equipment	25
a.	<i>Pump.....</i>	<i>25</i>
b.	<i>Connecting Hoses</i>	<i>25</i>
c.	<i>Pressure Monitoring and Protection.....</i>	<i>25</i>
d.	<i>Flow Measurement</i>	<i>26</i>
e.	<i>Displacement Measurement</i>	<i>26</i>
E.	TESTING SETUP AND EXPERIMENTAL METHODS	27
1.	Fluid Flow Test.....	27
2.	Corrosion Test.....	27
a.	<i>Samples.....</i>	<i>27</i>
b.	<i>Experimental setup</i>	<i>29</i>
III.	RESULTS	31
A.	FLUID FLOW TESTS	31
1.	Visual Observations.....	31

2.	Plate Displacements	34
B.	CORROSION TEST	42
1.	Visual Observations	42
2.	Mass Measurements.....	47
IV.	CONCLUSIONS AND RECOMMENDATIONS.....	51
A.	CONCLUSIONS	51
B.	RECOMMENDATIONS.....	52
APPENDIX. SENSOR CALIBRATIONS		53
LIST OF REFERENCES		55
INITIAL DISTRIBUTION LIST		59

LIST OF FIGURES

Figure 1.	Self-Cleaning Action on a Superhydrophobic Surface. Source: [6]	1
Figure 2.	Cassie-Baxter State. Source: [7]	2
Figure 3.	Hierarchical Surface Structure. Source: [7]	3
Figure 4.	Diagram of Slip at Solid-Fluid Interface. Source: [11]	3
Figure 5.	(Right) Image of Nanograss 7 μ m Tall, Spaced 1.25 μ m Apart, (Left) Image of Nanobricks 4 μ m Wide x 10 μ m Long and 1 μ m Tall. Source: [23]	5
Figure 6.	Laminar and Turbulent Flow Diagrams. Source: [28]	9
Figure 7.	Initial Design for Water Channel.	10
Figure 8.	Sample of Hexagonal Honeycomb Flow Conditioner.	11
Figure 9.	Example of Hole Placement for Securing Bolts.	12
Figure 10.	Partial Channel Assembly for Fitment Assessment.	13
Figure 11.	Removable Top for Flow Channel.	14
Figure 12.	Assembled Water Channel.	15
Figure 13.	Assembled Specimen Fixture Stand.	16
Figure 14.	Original Concept for Specimen Fixture.	17
Figure 15.	Parallel Pendulum Specimen Fixture.	18
Figure 16.	CAD Model of Cantilever Sensor.	20
Figure 17.	Sensor Response During Initial Testing Of the Cantilever System.	21
Figure 18.	Straked Cantilever.	22
Figure 19.	Comparison Between a Staked Cantilever and Bare Cantilever at Various Pump Speeds.	22
Figure 20.	Assembled Cantilever System in the Specimen Fixture.	23
Figure 21.	Test Stand Core with Channel and Pump.	24

Figure 22.	Completed Test Stand.	24
Figure 23.	Steel Spring and Mesh Vibration Isolation Mount.	25
Figure 24.	Assembled Testing Stand and Water Channel.	26
Figure 25.	SEM Imaging of Samples: Left Superhydrophobic, Middle Superhydrophilic, Right Untreated.	29
Figure 26.	FLSP Plate Fully Submersed in Water.	31
Figure 27.	Untreated Plate Fully Submersed in Water.	32
Figure 28.	FLSP Plate Immediately After Channel Draining.	33
Figure 29.	Plate Comparative Directly After Channel Draining.	33
Figure 30.	Sensor Voltage Output at 0 RPM.	35
Figure 31.	Displacement of Plates for 1100 RPM.	36
Figure 32.	Displacement of Plates for 1500 RPM.	37
Figure 33.	Displacement of Plates for 2000 RPM.	37
Figure 34.	Displacement of Plates for 2500 RPM.	38
Figure 35.	Displacement of Plates for 3000 RPM.	38
Figure 36.	Displacement of Plates for 3450 RPM.	39
Figure 37.	Difference in Displacement Between Test Plates.	39
Figure 38.	Force Exerted on Test Plates.	41
Figure 39.	Reduction in Force due to Superhydrophobic Surface.	41
Figure 40.	Corrosion Test Week 1, Left Superhydrophobic, Middle Superhydrophilic, Right Untreated.	42
Figure 41.	Corrosion Test Week 2, Left Superhydrophobic, Middle Superhydrophilic, Right Untreated.	43
Figure 42.	Corrosion Test Week 3, Left Superhydrophobic, Middle Superhydrophilic, Right Untreated.	44
Figure 43.	Corrosion Test Week 4, Left Superhydrophobic, Middle Superhydrophilic, Right Untreated.	44

Figure 44.	Corrosion Test Week 4 Magnified View, Left Superhydrophobic, Right Superhydrophilic.....	45
Figure 45.	Corrosion Test Week 5, Left Superhydrophobic, Middle Superhydrophilic, Right Untreated.	45
Figure 46.	Corrosion Test Week 6, Left Superhydrophobic, Middle Superhydrophilic, Right Untreated.	46
Figure 47.	Corrosion Test Week 6 Magnified View, Left Superhydrophobic, Middle Superhydrophilic, Right Untreated.....	47
Figure 48.	Superhydrophobic Sample Mass Over Time.	48
Figure 49.	Superhydrophilic Sample Mass Over Time.	48
Figure 50.	Untreated Sample Mass Over Time.	49

THIS PAGE INTENTIONALLY LEFT BLANK

LIST OF TABLES

Table 1.	EDS results, Weight % by Element.	28
Table 2.	Parameters Associated with Pump Speed.	34
Table 3.	Force and Sensor Displacement Values.....	40
Table 4.	Reduction in Skin Friction Force as a Result of Superhydrophobic Surface.	42
Table 5.	Weekly Mass Measurements For Corrosion Samples.	47

THIS PAGE INTENTIONALLY LEFT BLANK

ACKNOWLEDGMENTS

I would like to thank Professors Kwon, Didoszak, Mennon, and Park for their assistance and guidance throughout my research. I would also like to thank Professor Hobson for giving me free use of the school's machine shop, enabling me to construct the testing equipment myself.

Finally, I would like to thank my wife for her patience throughout my research, especially after the birth of our daughter.

THIS PAGE INTENTIONALLY LEFT BLANK

I. INTRODUCTION

A. BACKGROUND

In an economically driven world, great emphasis is always placed on engineers to design a system that is the most efficient it can be without sacrificing its intended purpose in order to reduce operating costs. The U.S. Navy spends millions of dollars a year in operational costs such as fuel, corrosion prevention, and biofouling remediation [1]. In an attempt to reduce operating costs, the Office of Naval Research (ONR) is continually searching for new methods and materials to increase the efficiency of current systems.

One such material of particular interest for the U.S. Navy's aqueous environment is one that exhibits superhydrophobic properties. A material is said to be superhydrophobic if the equilibrium contact angle of a water droplet is greater than 150 degrees and the contact hysteresis angle is less than 10 degrees [2]. The idea of extending superhydrophobic properties to a range of materials was first inspired by observing the water repelling and self-cleaning effects of the lotus leaf [3] and a number of other leaves found in nature [4]. Due to the large contact angle, the water droplets center of mass is moved further above the surface causing the droplets to have a rolling action rather than a sliding action [5], this combined with the more uniform surface tension of spherical geometry allows particles to become trapped in the droplet and carried away as seen in Figure 1.

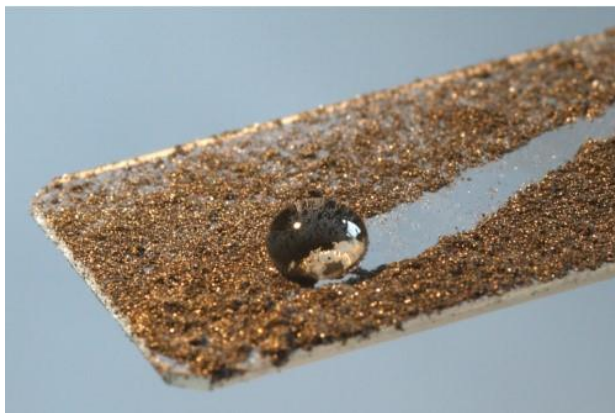


Figure 1. Self-Cleaning Action on a Superhydrophobic Surface. Source: [6]

Another important parameter of the superhydrophobic condition, and the primary area of focus for this study, comes from understanding how, in the Cassie state, a material can attain large enough contact angles to be considered superhydrophobic. When looking at the microscale roughness of a surface, if the distance between peaks is such that the static pressure of the water is not capable of overcoming the surface tension of the droplet, the valley will not become wetted. This results in an air-water interface at the material surface [8].

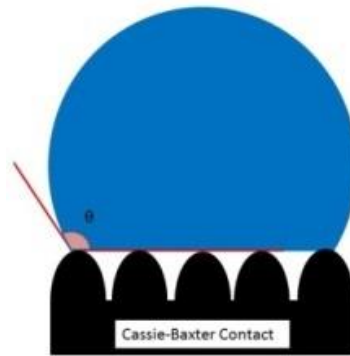


Figure 2. Cassie-Baxter State. Source: [7]

It can be seen from Figure 2, that in the Cassie state the equilibrium contact angle is a result of the proportion to the air-water interface. Revisiting the Lotus leaf effect, when the microscale peaks are combined with nanoscale features, a hierarchical structure is created and the Cassie state is improved by increasing the proportion of the air-water interface and thus increasing the equilibrium contact angle, thereby creating a surface that is near perfectly superhydrophobic, as seen in Figure 3. It is this air-water interface that is of particular interest to researchers and engineers, because of the potential to change fluid-surface interaction by the addition of an air film separation between the surface and the water and therefore altering the hydrodynamic properties.

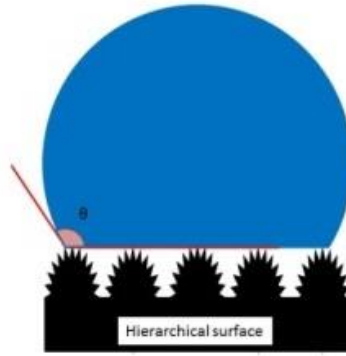


Figure 3. Hierarchical Surface Structure. Source: [7]

B. PRIOR RESEARCH

The concept of a no-slip boundary condition at the interface of fluid and surface is one that has been universally accepted and shown to be valid as a boundary condition through multiple studies. However, it should be noted that this boundary condition is one of an approximation that has been found to hold true for most normal flow conditions and therefore lends itself well for use in calculation and modeling [9]. Navier [10] was the first to hypothesize about the existence of a slip boundary condition, where he concluded that the slip velocity was proportional to the shear rate of the fluid amplified by the slip length. Figure 4 illustrates the idea of a slip velocity.

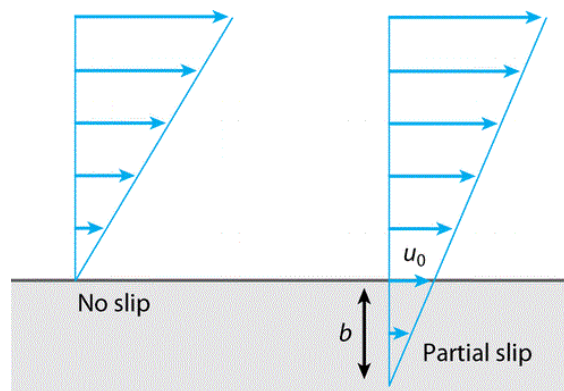


Figure 4. Diagram of Slip at Solid-Fluid Interface. Source: [11]

The concept of a slip boundary condition becomes important when realizing that if a fluid does not come to rest at the interface of a solid, momentum from the fluid will not be transferred to the solid, and energy loss from the bulk fluid can be avoided. In simple terms, this means the resistive force of drag can be reduced, consequently increasing the efficiency of the system. The mechanism by which this slip boundary condition is formed stems from the “lotus effect,” from the hierarchical surface structure of superhydrophobic materials. Recall that in a hierarchical surface under a Cassie state there resides a layer of air that separates the solid surface from the water. Because the dynamic viscosity of air is two orders of magnitude smaller than water, the hydrodynamic skin friction is greatly reduced and the water is said to slip over the air layer [12].

A number of direct numerical simulations (DNS) [13–16] and computational fluid dynamic (CFD) simulations [17–19] have shown that given the condition of superhydrophobicity at the surface there could be a significant increase in slip length, resulting in higher slip velocities. Martell theorizes that wall shear stress could be reduced as much as 50%, significantly reducing skin friction drag [15–16]. The results of these simulations are supported by experimental data as well. Fukuda et al. [20] and later Elbing et al. [21] experimented by injecting an air layer over a fully submerged body to create a thin air film over the surface. This is considered an active method for achieving the same hydrodynamic benefits as a superhydrophobic surface due to the added complication of manually adding an air film layer. Elbing et al. [21] showed that with a continuous air film at higher injection rates near complete elimination of skin friction drag occurred.

Due to the added complications, and the inherent increase in required energy for implementation, active systems may not be a practical means of reducing drag. It is therefore important to investigate materials where in the passive state exhibit the desired qualities of superhydrophobicity. It has been understood for some time that the degree of micro-scale surface roughness greatly contributes to the degree of hydrophobicity [22]. This knowledge, coupled with the ability to assemble and alter surfaces on the micro and nano-scale has given rise for the opportunity of manufacturing and experimental study.

Henoch et al. [23] was able to utilize photolithography to create structures on silicon wafers known as nanograss and nanobricks, seen in Figure 5.

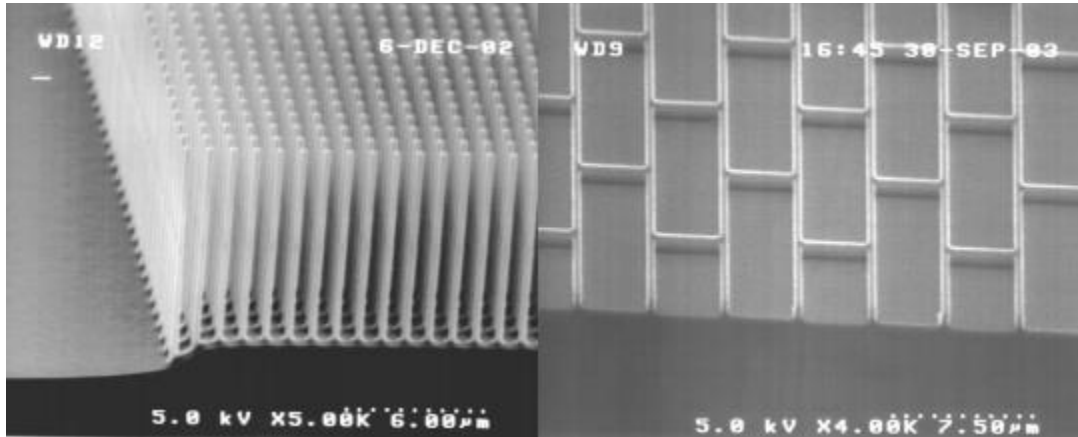


Figure 5. (Right) Image of Nanograss 7 μ m Tall, Spaced 1.25 μ m Apart, (Left) Image of Nanobricks 4 μ m Wide x 10 μ m Long and 1 μ m Tall.
Source: [23]

These structures were later coated with CF_x by plasma vapor deposition to obtain the desired superhydrophobic properties. The silicon wafers were then assembled into a rectangular form and submerged in a water tunnel for flow testing, the results of which showed a significant reduction in drag at all fluid velocities tested, and as much as 50% in the laminar region.

Furthering the field of study, Daniello et al. [24] used a similar lithographic process to create silicon wafer molds in which polydimethylsiloxane (PDMS) was cast into 150 mm long patches, and then seamlessly joined to create a 1 m long superhydrophobic surface. These plates were assembled into a rectangular flow channel in which they performed pressure drop measurements, and particle image velocimetry, (PIV) over a range of Reynolds numbers from laminar to turbulent. The results of his study show there is a measurable decrease in drag that becomes prominent in the turbulent region. Daniello et al. [24] hypothesizes, that in the turbulent region the reduction in drag is proportional to the Reynolds number and therefore to the thickness of the viscous sublayer. The results also suggest there is an asymptotic limit in drag

reduction where the thickness of the viscous sublayer decreases to less than the height of the micro ridges for the surface topology. This would result in the sudden onset of micro roughness being exposed to the flow causing a hold on drag reduction.

In more recent years, with the development of micro and nano-scaled chemical coatings, it has become more economically and commercially viable to treat the surface of a material, to achieve properties that are not naturally present. Aljallis et al. [25] conducted a study in which two aluminum plates, (length, width, thickness = 1.2192m (48in), 0.635m (24in), 0.009525m (3/8in)) with sharpened leading and trailing edges in order to reduce form drag, were spray coated with an acrylic base and two different types of hydrophobic nano-particles (samples SH-1 and SH-2). The difference between the two types is that one of the base coats contained micro-particles (SH-2). The two plates, along with an uncoated control plate were then run through a tow tank at both laminar and turbulent velocities. The results of their study showed that in all flow velocities the plate designated as SH-1 displayed a higher drag coefficient than the control plate, while SH-2 showed reduced drag at lower velocities and no significant change from the control plate at higher velocities. These results point to the conclusion that coating systems are not a viable option for drag reduction in practical applications.

C. RECENT DEVELOPMENTS

To date, the studies that have tested the theory of reduced skin friction drag due to superhydrophobic surface conditions have been limited to samples that were manufactured by means of photolithography and made out of silicone and its derivatives [23-24], which have limited engineering applications; or polymer-based coatings [25] which have questionable reliability and curability.

With the use of femto-second laser surface processing (FLSP), functionalizing the surface of metallic substrates through ablation became possible. Through the control of wave length, pulse length, and fluence, the creation of micro and nano-scaled features on metallic surfaces could be produced to resemble the silicon and polymer coating surfaces mentioned above. Kietzig et al. [26] was able to produce functionalized surfaces over varying metallic substrates in order to study the change in surface properties as it pertains

to water adhesion. As discussed in the study, it was found that by varying the fluence of the laser, the granularity and the average surface roughness could be greatly changed. With increasing fluence came in increase in average surface roughness. It was also noted that samples directly after surface processing exhibited superhydrophilic properties with contact angles less than 20 degrees. However, when the samples were allowed to rest in normal atmosphere, or in a carbon dioxide rich atmosphere, it was noted that soon after surface properties exhibited hydrophobic or superhydrophobic characteristics. The length of time required for the change in properties is proportional to the fluence. After performing Elemental Surface Analysis (XPS) to monitor the change in surface chemistry following functionalization, Kietzig et al. [26] observed that there was a dramatic increase in the presence carbon. This was attributed to the creation of a nonstoichiometric oxygen deficient iron oxide scale (active magnetite, $\text{Fe}_3\text{O}_{4-\delta}$). The presence of this magnetite caused the catalyzation and dissociative absorption of carbon dioxide. Carbon dioxide becomes zero valence carbon monoxide and oxygen anions diffuse into lattice vacancies to form stoichiometric Fe_3O_4 . This causes the gradual accumulation of nonpolar carbon on the rough dual scale surface, and in conjunction, create a surface topography that is superhydrophobic.

Furthering this research, Zuhlke et al. [27] using FLSP, created stainless steel and titanium samples with three different surface topographies, Below Surface Growth mounds (BSG-mounds), Above Surface Growth mounds (ASG-mounds), and Nanoparticle Covered pyramids (NC-pyramids). The scope of this study was to determine the longevity of the air film attached to the surface while submerged in water and synthetic stomach acid. Each sample created attained initial wetting angles greater than 160 degrees while the stainless steel samples had a better performance. The results of the study showed that stainless steel in the ASG or BSG-mound configuration could maintain an air film for over 30 days, and didn't reach full degradation until 39 days in the case of BSG-mounds and greater than 41 days for ASG-mounds.

Due to the resiliency and durability of metal over silicon structures and polymer coatings, FLSP functionalized metallic substrates offer a practical engineering material that can be used in commercial applications where superhydrophobic properties are

desirable such as reducing drag on the hull of a ship, which in turn lowers the amount of fuel consumed..

D. OBJECTIVE

The objective of this research is to construct a water tunnel testing stand capable holding parallel samples for comparative analysis of air film retention over a range of Reynolds numbers, and flow characteristics, as well as determination of the difference in skin friction drag between a treated and untreated flat plate sample. In parallel, samples will also be placed in a salt fog chamber and monitored for the progression of corrosion to determine the resiliency of FLSP functionalization. Ultimately, the goal of this research is to provide insight into the commercial viability of integrating these materials into areas that would benefit from self-cleaning low hydrodynamic drag applications.

II. FABRICATION AND EXPERIMENTAL METHODS

A. WATER TUNNEL DESIGN AND FABRICATION

The basis for the design of the water tunnel was to allow for observation and sensor measurements of fully submerged specimens in a uniform flow at various speeds. Additionally, it was desired to run two specimens in parallel allowing for a control group specimen to provide a baseline under the same conditions as a treated specimen. The sizing of the tunnel was chosen such that there would be no wall interactions with the specimens. To ensure this, the flow velocity of the water is such that a transitional and turbulent Reynolds number is achieved. Because the flow is turbulent, the velocity profile in the vicinity of the specimens is more uniform with little influence from the viscous sublayer of the tunnel walls. The more uniform velocity of turbulent flow can be clearly seen in Figure 6.

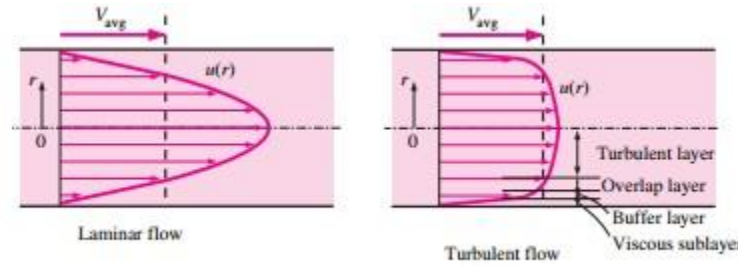


Figure 6. Laminar and Turbulent Flow Diagrams. Source: [28]

1. Channel Design

The water channel was machined and assembled from 25.4 mm (1 in) thick cast acrylic, however the actual thickness of the material provided was an average of 23.622 mm (0.930 in) with a variance of 0.0762 mm (0.003 in). The overall initial design of the channel can be seen in Figure 7.

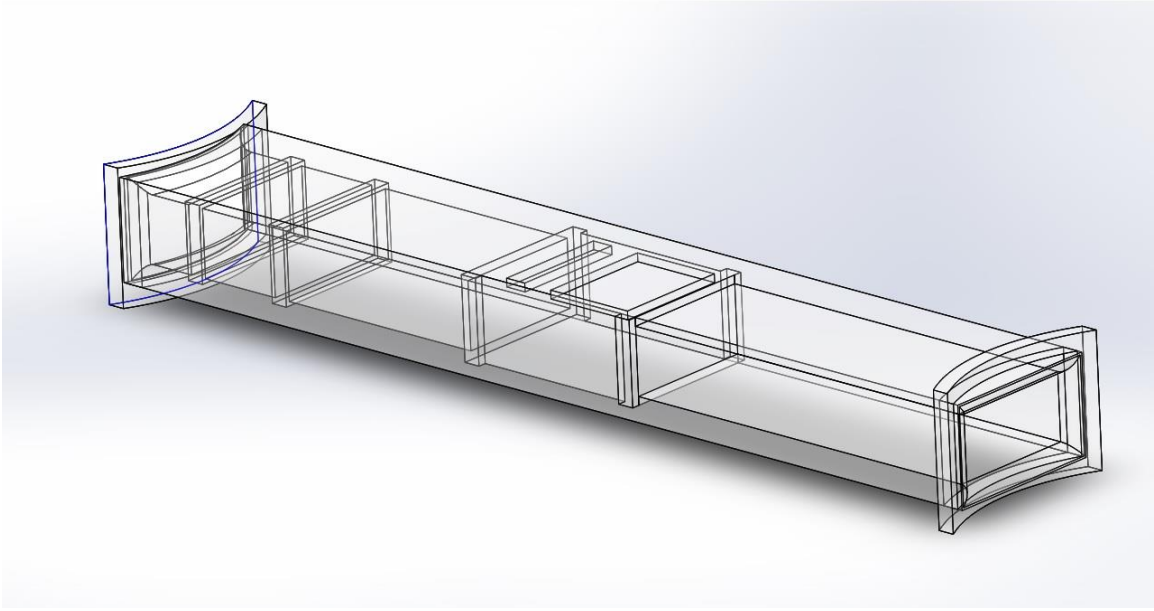


Figure 7. Initial Design for Water Channel.

The channel interior dimensions measure, 101.6 mm (4 in) tall by 203.2 mm (8 in) wide with a length of 1524 mm (60 in). The negative profile cut into the interior at the approximate mid span location is introduced so that the specimen fixture may be flush mounted into the channel, thereby not influencing the flow. The two negative profiles cut into the interior of the channel toward the entrance are for honeycomb-structured flow conditioners.

The design flow volume for this channel is selectable between 227.12 l/min (60 gpm) and 832.79 l/min (220 gpm). Using the following equation a range of Reynolds numbers was established.

$$\text{Re} = \frac{D_h \rho u}{\mu} \quad (1)$$

Where D_h is the hydraulic diameter, ρ is the density of water at 20° C (68° F), u is the free stream velocity, and μ is the dynamic viscosity of water. Using the flows mentioned above the expected span of channel Reynolds numbers is between 24,780 and 91,031. This range correlates to the turbulent region for pipe flow, therefore flow conditioners

were implemented into the design to limit the velocity vector such that it is coincident with the length of the channel.

The two flow conditioners measuring 114.3 mm (4.5 in) tall, 215.9 mm (8.5 in) wide, and 25.4 mm (1 in) thick, are placed 203.2 mm (8 in) from the entrance of the channel and 152.4 mm (6 in) apart. The honeycomb is made up of hexagons measuring 5.842 mm (0.23 in) from corner to corner and 5.08 mm (0.2 in) from side to side. The effect of the flow conditioners is twofold; the primary purpose is to create a uniform single vector flow coincident with the channel length. The secondary purpose is to facilitate a pressure drop in the downstream specimen testing region. The reduced pressure is desired to protect the gaskets lining the removable cover over the specimen fixture from potential leaks. Figure 8 shows the structure of the flow conditioners.



Figure 8. Sample of Hexagonal Honeycomb Flow Conditioner.

The channel was made from 6 pieces. The bottom measured 254 mm (10 in) wide and 1524 mm (60 in) long, and the two sides were 101.6 mm (4 in) by 1524 mm (60 in). The top was divided into 3 pieces, each measuring 254 mm (10 in) by 508 mm (20 in). The middle section, which is removable, was then shortened by 3.175 mm (0.125 in) to allow for the placement of a gasket while maintaining the combined length of 1524 mm (60 in). In the top and bottom sections, 8.2042mm (0.323 in) diameter holes were drilled

through the thickness, the positions of which were starting 25.4mm (1 in) in from the end, 13.589 mm (0.535 in) from the side, and repeated every 50.8 mm (2 in) for the length of the sections. On the exterior surface, the holes were then countersunk with a standard 82° bit to allow for flush mounting of the 5/16-18 National Course (NC) stainless steel hex drive cap screws. Figure 9 illustrates hole placements and countersinking.



Figure 9. Example of Hole Placement for Securing Bolts.

The side sections were then drilled with a 6.5278 mm (0.257 in) diameter bit down the centerline of the thickness starting 25.4 mm (1 in) from the end and every 50.8 mm (2 in) thereafter to align with the top and bottom sections. The depth of the hole was limited to 44.45 mm (1.75 in). The holes were then tapped using a standard 5/16-18 NC bit. The negative profiles for the honeycomb flow conditioners were milled into the acrylic using a 25.4 mm (1 in) two fluted end mill. The position of the cuts were 203.2 mm (8 in) from the entrance of the tunnel and 152.4 mm (6 in) apart. The depth of cut was 6.35 mm (0.25 in). For the side pieces, the cut spanned the entire width while in the

top and bottom pieces 19.05 mm (0.75 in) of acrylic was left at the ends of the cut. For the top and bottom pieces, the ends were then squared off by chisel to allow for the rectangular profile of the flow conditioners. A similar technique was used to mill the negative profile for the specimen fixture, with the leading edge of the fixture positioned 711.2 mm (28 in) from the entrance of the channel.

Figure 10 shows the bottom and sides assembled with the flow conditioners and specimen fixture in place for fitment assessment. In joining the pieces, prior to bolt installation, a clear silicon sealant was applied to create a watertight joint.

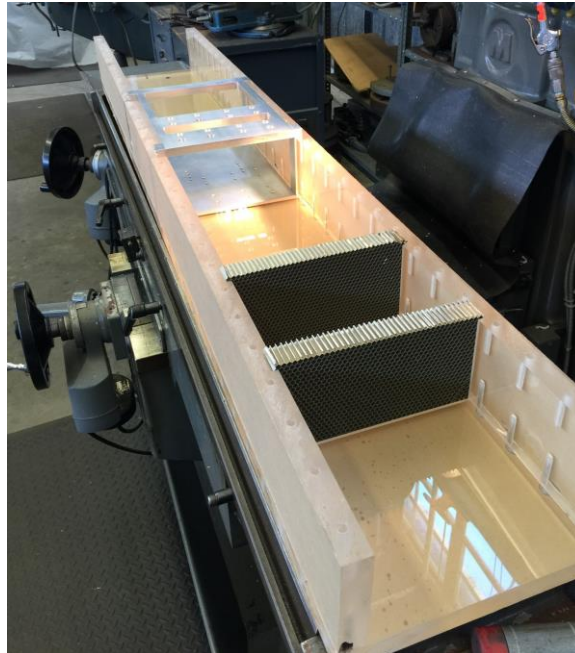


Figure 10. Partial Channel Assembly for Fitment Assessment.

Once the channel was assembled, the entrance and exit were modified to remove the 90° edge. A 22.225 mm (0.875 in) fillet was milled along the channels entrance and exit inside perimeter to reduce losses and promote more stable flow conditions.

2. Removable Top Design

As mentioned above, the top is composed of three sections. The two permanently mounted sections measure 254 mm (10 in) wide and 508 mm (20 in) long, are assembled

in an identical manner as the bottom and sides. The removable middle top section measures 3.175 mm (0.125 in) shorter in length to accommodate the gasket for sealing. A 3.175 mm (0.125 in) diameter rubber gasket is inlaid to a depth of one-half the diameter into the removable top and routed 3.175 mm (0.125 in) away from the perimeter of the negative profile. Figure 11 shows the design of the removable top.



Figure 11. Removable Top for Flow Channel.

3. Receiving Fixture Design

In order to facilitate connecting the channel to the upstream and downstream reservoirs a curved receiving fixture was milled on a CNC machine and attached to the ends of the channel. Each receiving fixture consisted of four pieces. The top and bottom have a square 25.4 x 25.4 mm (1 x 1 in) cross section with a mean radius of curvature of 301.498 mm (11.875 in) and a chord length of 304.8 mm (12 in). The two sides consist of a parallelogram with cross sectional measurements of 28.702 x 28.702 mm (1.13 x 1.13 in), major and minor angles of 117.69° and 62.31°, and a height of 101.6 mm (4 in). The pieces of the fixture were then assembled and mounted to the channel using SCIGRIP 4 acrylic cement.

Figure 12 shows the completed pieces of the water channel assembled prior to the installation of the up and downstream reservoirs, framing stand, and ancillary equipment.



Figure 12. Assembled Water Channel.

B. SPECIMEN FIXTURE DESIGN AND FABRICATION

The main design goal behind the specimen fixture was adaptability. To accommodate this, the fixture is removable and modular. The fixture consists of six main pieces milled from 12.7 mm (0.5 in) thick aluminum. The four side pieces have cross sectional dimensions of 25.4 x 12.7 mm (1 x 0.5 in) and a height of 127 mm (5 in). The top and bottom have dimensions of 304.8 x 203.2 x 12.7 mm (12 x 8 x 0.5 in) L x W x T. The sides were bolted to the top and bottom with two ¼-20 x 1 in socket head cap screws

on each end to prevent the possibility of rotation about the connecting points. Figure 13 shows the fixture in its assembled state.

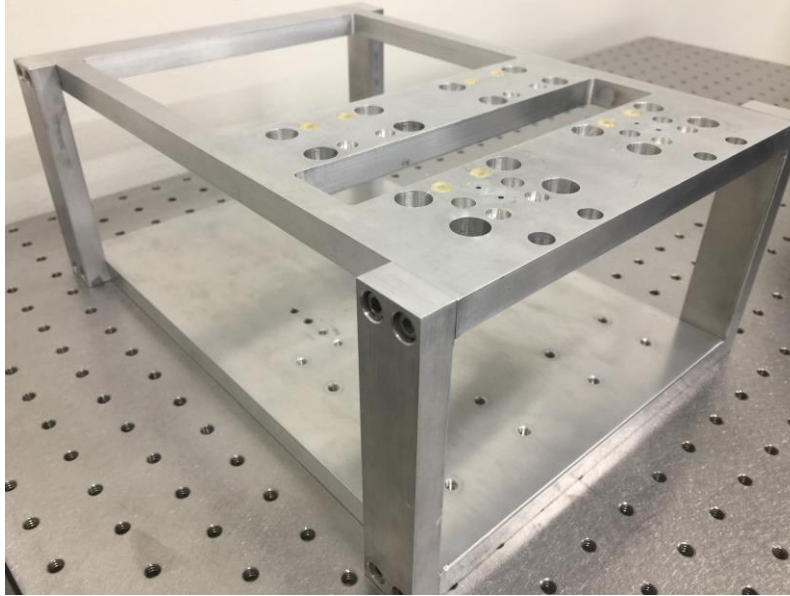


Figure 13. Assembled Specimen Fixture Stand.

The hole placements and patterns in both the top and bottom plates were arranged for multiple possible specimen and sensor setups, however both top and bottom are replaceable should a need for a different arrangement arise.

1. Initial Concept

The original design called for both a FLSP treated plate and untreated plate to be suspended and constrained (with the exception of in the direction of flow), by eight 40 mm (1.57 in) styli with a 1.5 mm (0.059 in) ruby sphere. The plates would be suspended at approximately 50% of the height of the channel, separated by 25.4 mm (1 in) and have 25.4 mm (1 in) clearance from the channel walls. These offset distances insure there are no boundary layer interactions between the walls and test specimens. A displacement sensor with a 0.2 N/mm spring force was to be placed directly behind the center of each plate. However, during static friction determination to find the force necessary for the inception of movement for each, plate it was found that the untreated plate required 0.423

N of force while the treated plate required 1.177 N of Force. In its current condition the maximum flow velocity attainable in the channel is 0.6723 m/sec (2.21 ft/sec). To estimate the expected force imparted on the plates due to fluid flow, equation (2) was used.

$$F_d = \frac{1}{2} \rho u^2 c_d A \quad (2)$$

Where c_d is the coefficient of drag for a flat plate perpendicular to flow estimated at 1.1, and A is the area of the plate seen by the flow. This equates to an estimated force of 0.0451 N which is far below the force required to overcome static friction, therefore an alternate means of specimen fixturing was devised. Figure 14 shows the original specimen fixture design.

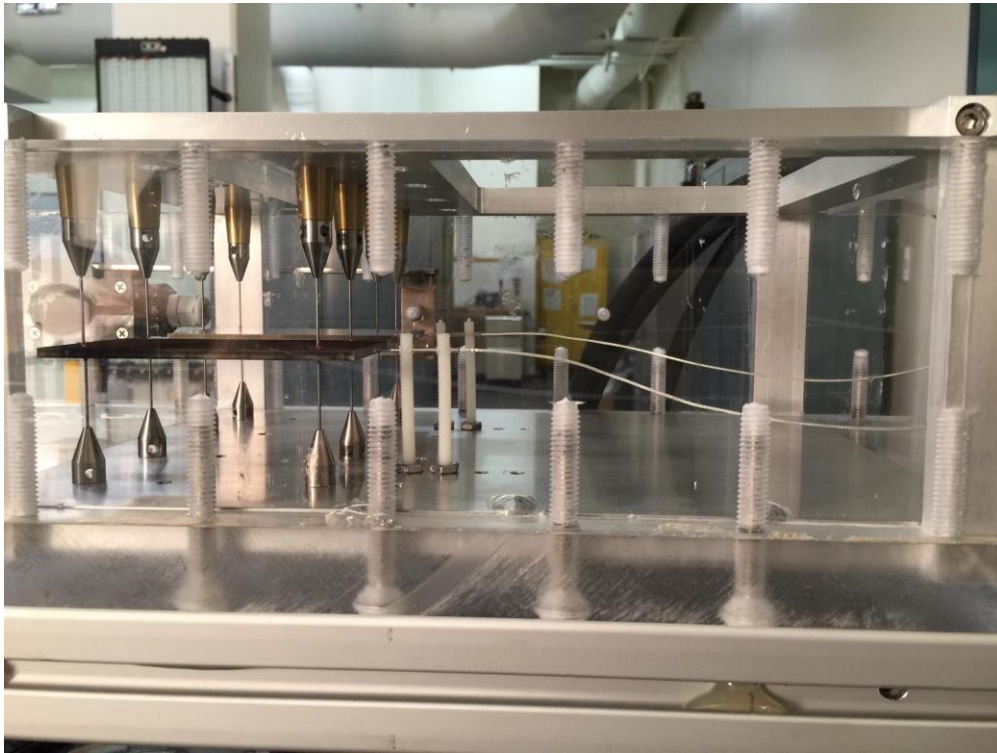


Figure 14. Original Concept for Specimen Fixture.

2. Final Design

In order to minimize the presence of sliding friction to a negligible level the use of a parallel pendulum setup was incorporated. Using 0.1016 mm (0.004 in) polymer wire, two loops were attached to the top of the specimen fixture and extended down around the plate at a suspension height of 40 mm (1.57 in) from the bottom of the channel. With the pendulum length of 61.595 mm (2.425 in), and an estimated force of 0.0451 N, given the mass of the plate, the resulting angle of deflection is less than 2 degrees. Therefore, the motion of the plate can be approximated as linear horizontal since the vertical displacement is 0.032 mm (0.0013 in). Figure 15 shows the parallel pendulum setup with the plates in place.

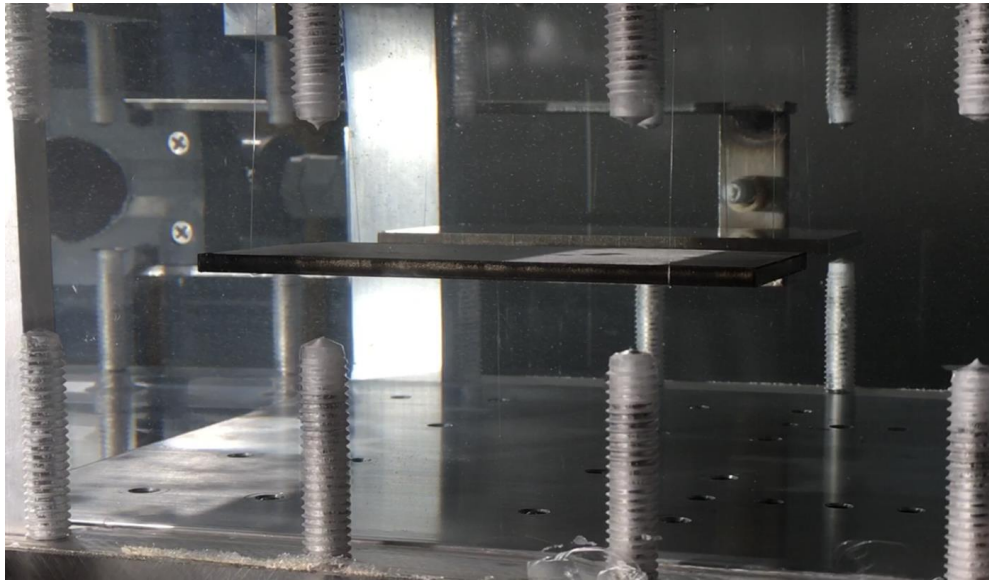


Figure 15. Parallel Pendulum Specimen Fixture.

C. SENSOR DESIGN, FABRICATION, AND INTEGRATION

In order to facilitate the measurement of forces in the range of millinewtons or less, a highly sensitive displacement sensor with a known spring constant was utilized. The Lord Microminiature Gauging DVRT [29] in the high-resolution setup is capable of a 300 nm resolution with a 0.2 N/mm spring constant. Using the estimated force of

0.0451 N an expected displacement of 0.2255 mm (0.00888 in) can be achieved, which is well within the measurability of this sensor.

1. Initial Concept

After receiving the sensors and verifying the calibration, it was discovered there was a sizable dead zone in the beginning of the stroke. The force to overcome the dead zone and enter the linear output signal zone between the two sensors averaged 0.2113 N. This force is over 4 times greater than the expected force imparted on the plates. Therefore, direct measurement of the displacements of the plates by the sensors was no longer feasible. The preloading condition that would be required to enter the linear output signal zone would displace the plates from their equilibrium position by an unacceptable amount. Therefore, an alternative system was developed that would make use of mechanical advantage.

2. Final Design

In order to fully utilize the high-resolution capabilities of the differential variable reluctance transducers (DVRT) a displacement compression method was introduced.

a. Preliminary Concept Design

Using linear elasticity a finite element analysis (FEA) model was developed in MATLAB to represent a linear elastic cantilever with a rigid contact pipe. Figure 16 represents the computer model of the cantilever.

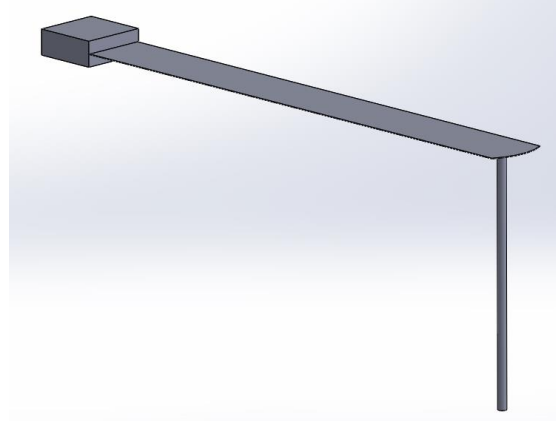


Figure 16. CAD Model of Cantilever Sensor.

The cantilever has dimensions of 12.7 mm (0.5 in) wide, and 139.7 mm (5.5 in) long. The rigid contacting pipe has a diameter of 1.778 mm (0.07 in) with a wall thickness of 0.381 mm (0.015 in) and is mounted along the center of the cantilever width and 5.5118 mm (0.217 in) from the free end. The overall length of the contacting pipe is 53.975 mm (2.125 in). Using a conservative approach, and assuming only 10% of the 0.0451 N force is transmitted to the rigid contact pipe, an iterative analysis of the FEA model was completed to determine the most effective cantilever thickness. After balancing the effects of the applied force, and the force due to preloading the sensor at a contact point of 20 mm (0.787 in) from the fixed end on the top side of the cantilever, it was decided that a thickness of 0.254 mm (0.01 in) would yield an adequate sensitivity without detrimental deformation from sensor preloading. Using a sensor preloading force of 0.3332 N and an applied force of 0.00451 N at the tip of the contact pipe the calculated beam deflection at the sensor would be 13 microns, well within the accuracy of the DVRT.

Upon initial testing of the cantilever in a flowing stream of water, it was discovered that vortex induced vibration (VIV) from the contact pipe caused significant instability in the cantilever system that was translated to the sensor. Figure 17 shows the voltage output of the sensor at various pump speeds.

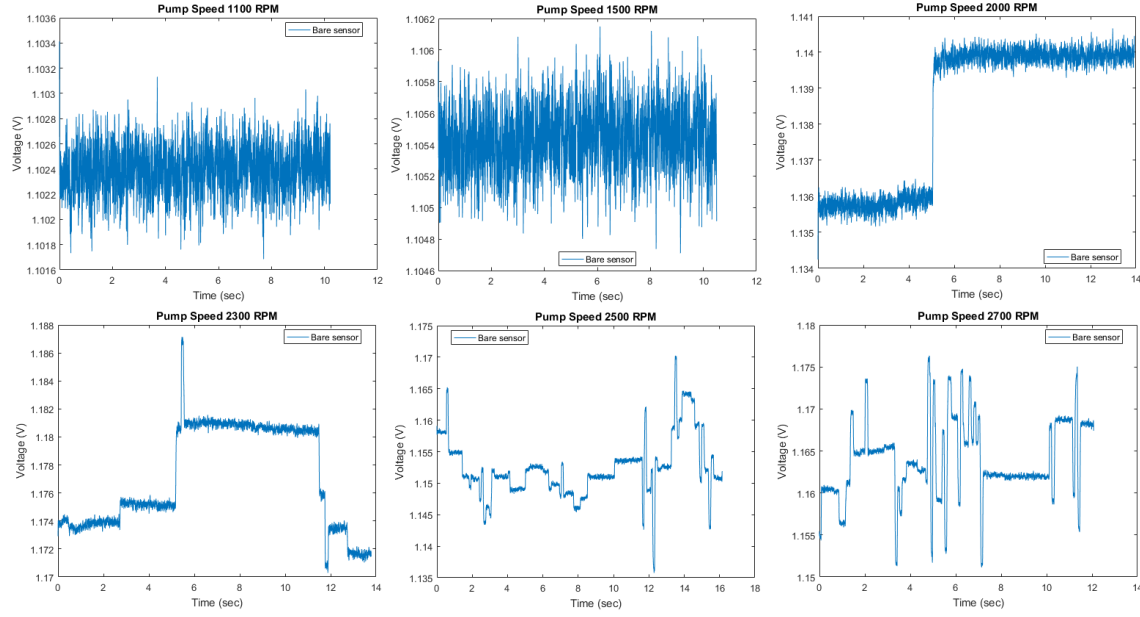


Figure 17. Sensor Response During Initial Testing Of the Cantilever System.

From this data it was determined that the irregularity of the sensor output due to VIV would preclude the possibility of obtaining accurate results, therefore, the use of strakes was introduced.

b. Practical Application Design

A strake is a device that is used to introduce turbulence around a cylindrical body thereby disrupting the formation of a Von Karman vortex street, the mechanism by which VIV is established. In a hydrodynamic environment, the ideal employment of this method requires the use of three strakes wrapped in a helical manner with a pitch of 17.5 times the diameter of the pipe and a height of 25% of the diameter of the pipe [30]. Due to the small diameter of the contact pipe, the use of three strakes was not practical, therefore, one strake was used and the pitch was divided by three to compensate. The final implementation used a polymer wire with a diameter of 0.4572 mm (0.018 in) wrapped around in a helical manner five times. Figure 18 shows the implementation of the strake described above.



Figure 18. Straked Cantilever.

With a straked cantilever completed, a test run was conducted whereby a straked and bare cantilever were run in parallel under the same flow conditions. Figure 19 shows the results of that run.

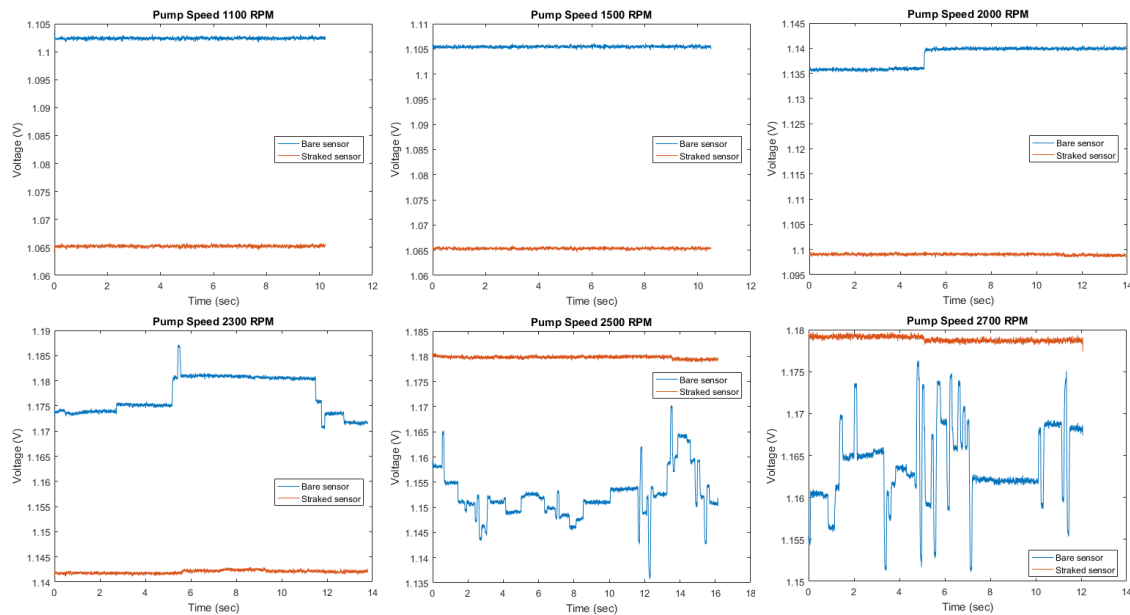


Figure 19. Comparison Between a Staked Cantilever and Bare Cantilever at Various Pump Speeds.

It was immediately determined that VIV was nearly eliminated for all pump speeds and that the stability of the cantilever system was now in an acceptable range for reliable displacement measurements. Figure 20 shows the final construction and assembly of the cantilever system mounted in the specimen fixture.

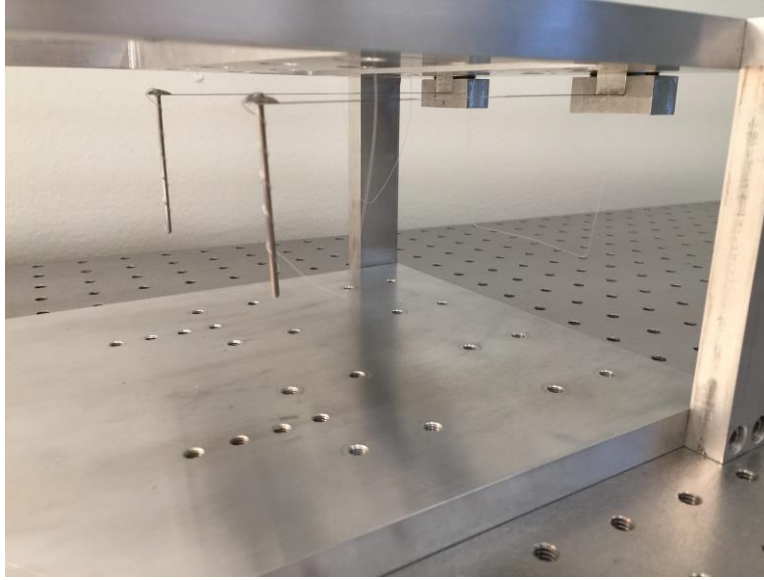


Figure 20. Assembled Cantilever System in the Specimen Fixture.

D. WATER CHANNEL TEST STAND AND ANCILLARY EQUIPMENT

1. Test Stand

To finish the water channel, a stand was developed with the goals of portability and compactness. A frame was developed to support the channel and the majority of the ancillary equipment. In Figure 21 is the frame with the channel and pump placed in position.

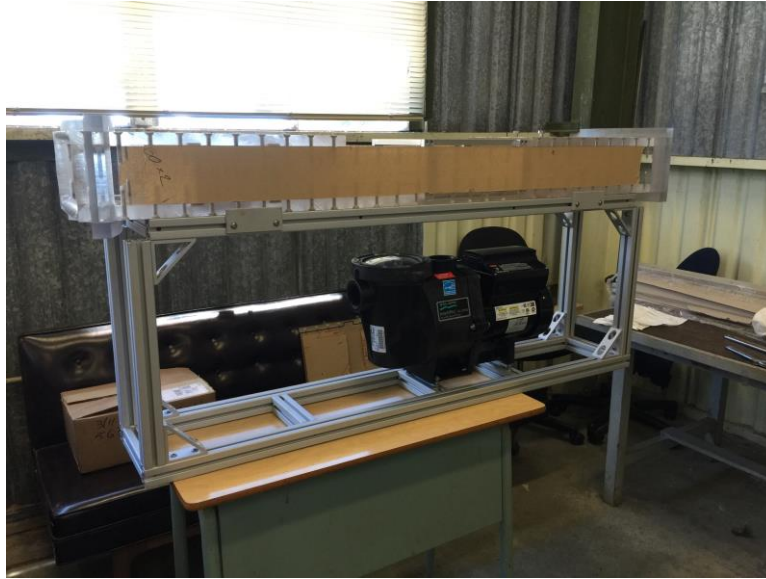


Figure 21. Test Stand Core with Channel and Pump.

Next, platforms were developed to support the upstream and downstream reservoirs, and a substructure was added to increase the rigidity of the stand, accommodating the large amount of mass added when filled for testing. Figure 22 shows the completion of the test stand.



Figure 22. Completed Test Stand.

2. Ancillary Equipment

a. Pump

The pump is a Sta-Rite Intellipro P6E6XS4H-209L VS+SVRS 3HP variable speed pump, with a flow range of 60 – 220 Gpm. The pump is mounted on four steel springs and mesh vibration isolation mounts pictured in Figure 23, with a maximum transmissibility of 0.5 for the testing operating range.



Figure 23. Steel Spring and Mesh Vibration Isolation Mount.

b. Connecting Hoses

The pump inlet and outlet is connected to the upstream and downstream reservoirs by 50.8 mm (2 in) smooth bore PVC clear piping with a rigid PVC helix. The pump side uses 50.8 mm (2 in) hose barb to threaded connection while the reservoir side uses hose barb to cam lever couplers.

c. Pressure Monitoring and Protection

The outlet of the pump is monitored by a high precision 0 – 206.8 kPa (0 – 30 psig) gauge and protected from over pressurization by a compact brass pressure regulator with a selectable range between 0 – 413.7 kPa (0 – 60 psig) which unloads directly to the inlet. The pump inlet is monitored by a 0 - 101.6 kPa (0 – 30 inHg) vacuum gauge.

d. Flow Measurement

The channel flow rate is measured using a Dynasonics ultrasonic clamp-on flow Meter with remote mounting display. The system is powered by an external 12 volt DC power supply mounted next to the outlet pressure gauge.

e. Displacement Measurement

As previously mentioned, the specimens displacement is measured by a cantilever system connected to a Lord Microminiature Gauging DVRT® [29] in the high resolution setup, capable of a 300 nm resolution. The DVRT is powered from the same source as the Dynasonics flow meter. The voltage output of the DVRT is recorded using a National Instruments ± 10 V, Analog Input, 500 kS/s, 8 Ch Module, model number NI 9201, along with a 4-slot CompactDAQ USB chassis model number cDAQ-9417.

Figure 24 shows assembled testing stand after initial operational tests.



Figure 24. Assembled Testing Stand and Water Channel.

E. TESTING SETUP AND EXPERIMENTAL METHODS

1. Fluid Flow Test

To initialize the setup, the cantilevers are mounted in their clamps with 0.25 mm (0.01 in) protruding from the fixed end. The specimens are then placed in the double pendulum swing at a position that is parallel to the base of the specimen fixture and the flow. They are then moved in the channels longitudinal direction until contact is made with the cantilevers contacting pipe, but not enough to deform the cantilever.

The specimen fixture is then carefully placed into the channel in a manner as not to disturb plate's positions. The DVRT sensors are then positioned to yield a 950 ± 50 mV output. Once the desired sensor preload has been obtained the cover is then set into place and bolted to the channel. The reservoirs are filled to approximately 50.8 mm (2 in) from the top with distilled water, and the fill ports are sealed.

The voltage output of the sensors is then recorded while the system is in a static condition to obtain the baseline position of the plates. The pump is initiated and voltage is recorded at various speeds for 30 seconds, following a five minute settling time to ensure flow has reached a uniform speed through the channel. At each pump speed, the channel flow rate is recorded to obtain the Reynolds number.

The displacements of the plates are then correlated to a force required for such a displacement and graphed against the Reynolds number.

2. Corrosion Test

In order to test the resiliency of functionalized surfaces compared to untreated samples with respect to environmental conditions, an accelerated corrosion method was used following ASTM-B117 standards.

a. Samples

The University of Nebraska-Lincoln's Laser Science Engineering Research Lab. provided 21 square 25.4 x 25.4 mm (1 x 1 in) samples. These samples consisted of three groups of seven; each group consisted of superhydrophobic, superhydrophilic, and

untreated samples. Each treated sample was prepared with the same FLSP parameters, the differing surface properties were obtained by the environmental conditions to which the samples were exposed directly after laser processing. As explained above, superhydrophobic samples were exposed to a carbon rich atmosphere, while superhydrophilic samples were exposed to a carbon deficient atmosphere.

The material classification was not provided to the University of Nebraska-Lincoln; therefore, Energy Dispersive X-ray Spectroscopy (EDS) was performed in order to determine the material. The following table shows the results for the elemental make up of a few selected samples.

Table 1. EDS Results, Weight % by Element.

Sample	MgK	AlK	SiK	TiK	CrK	MnK	FeK	CuK	ZnK
HVH17	4.38	93.79	0.13	0.10	0.18	0.85	0.37	0.12	0.08
HVG37	4.61	93.65	0.05	0.05	0.12	0.64	0.40	0.17	0.31
HVH1	4.46	93.64	0.14	0.08	0.15	0.84	0.36	0.16	0.17
HVG13	4.64	93.84	0.06	0.08	0.12	0.61	0.33	0.14	0.19
HVG1	4.45	94.18	0.05	0.06	0.10	0.63	0.26	0.10	0.17
HVH25	4.48	93.69	0.10	0.08	0.20	0.82	0.37	0.08	0.18

After analyzing the EDS results and within a 99% confidence level, the material in which all samples were prepared was determined to be aluminum 5083.

The samples were then imaged under an electron microscope to run a qualitative comparison of the surface topography between the three groups. The following image shows a sample of what was recorded, on the left is an example of a superhydrophobic sample. The middle shows a superhydrophilic sample, and the right is the untreated control sample.

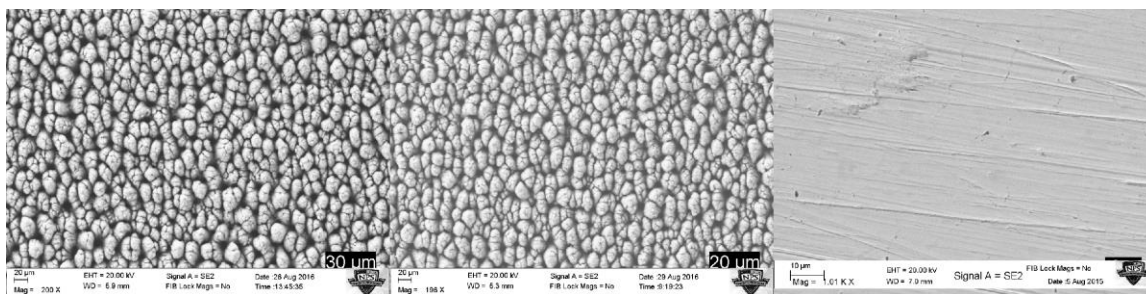


Figure 25. SEM Imaging of Samples: Left Superhydrophobic, Middle Superhydrophilic, Right Untreated.

From the images examined it was determined that the surface topography between the different FLSP samples were identical within the confines of a randomly generated self-organized below surface growth FLSP. This further reinforces the ideas mentioned above; it is the treatment directly following laser processing that determines wettability.

b. Experimental setup

Using an Associated Environmental Systems salt fog chamber model MX-9204, 21 samples were suspended to a height of 50% of the total enclosure height and exposed to an atmosphere consisting of an atomized 3.5% salt solution, and a temperature of 35°C. The samples were left in continuous contact with the atmosphere for 1000 hours, with the exception of 1 hour per week for observation and mass measurements. During the weekly observations, the surfaces of the samples were allowed to dry; however, no alterations were made. Each sample was suspended with a synthetic non-wicking material and aligned in three rows evenly spaced, each row consisting of superhydrophobic, superhydrophilic, and untreated samples. At the conclusion of the experiment, the samples were allowed to dry as normal for weight measurements and then cleaned with deionized water to remove excess salt deposits. Once the salt was removed, the samples were weighed a final time to obtain the overall weight difference.

THIS PAGE INTENTIONALLY LEFT BLANK

III. RESULTS

A. FLUID FLOW TESTS

A series of test runs were conducted with a FLSP treated plate and an untreated plate in parallel to ensure identical flow conditions. Data was recorded at pump speeds of 1100, 1500, 2000, 2500, 3000, and 3450 rpm. The tests were repeated multiple times while changing the positions of the plates, cantilevers, and sensors to ensure unbiased repeatability.

1. Visual Observations

Upon filling the channel with water, the superhydrophobic properties of the FLSP treated plate were immediately noticeable. A thin plastron (air) film formed around the plate having the appearance of a layer of ice with the surface texture of fine sand paper. Figure 26 shows an FLSP plate fully immersed in water.

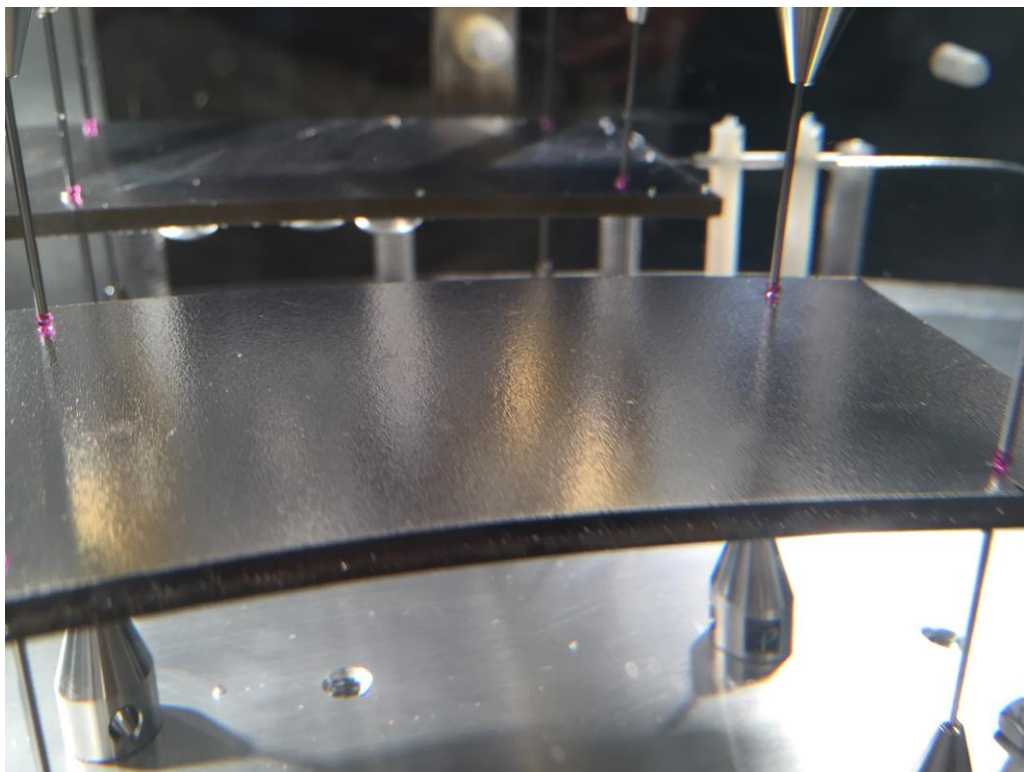


Figure 26. FLSP Plate Fully Submersed in Water.

For comparison, Figure 27 show a more clear view of the untreated plate seen in the background of figure 26.

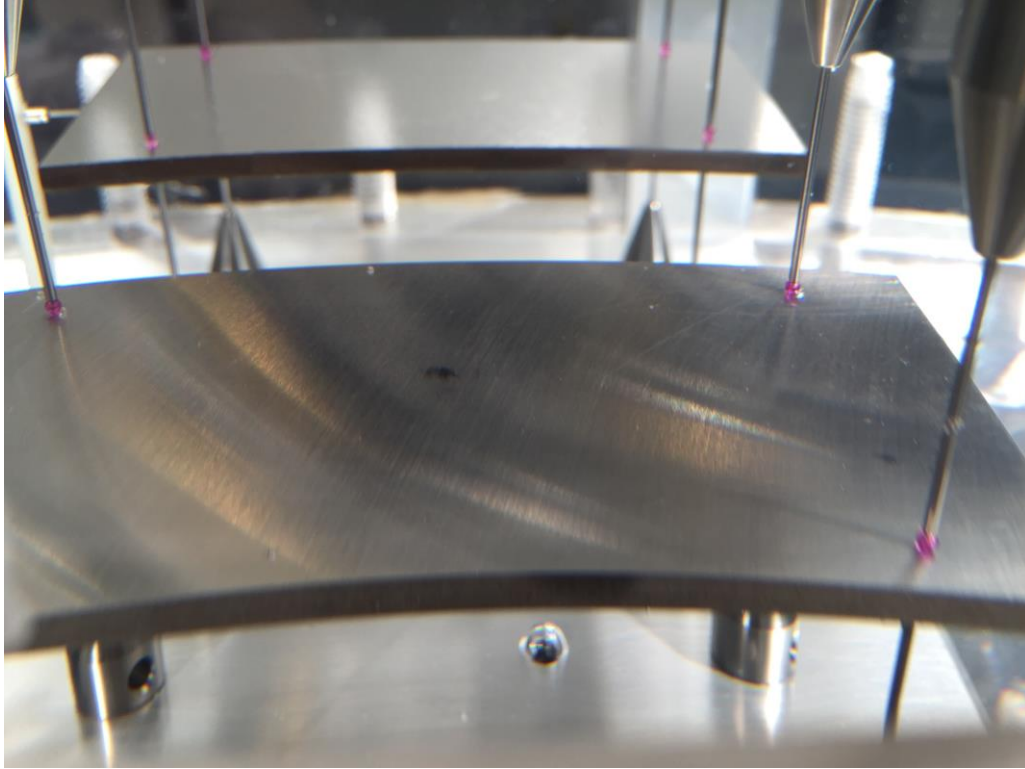


Figure 27. Untreated Plate Fully Submersed in Water.

From these two images, it becomes quite clear that the water never comes in physical contact with the surface of the FLSP plate, and to further support this, Figures 28 and 29 show the FLSP plate directly after the system was run at full speed for 10 minutes and the channel drained. Also notable, was the plastron layer showed remarkable stability at all channel velocities. There was never an indication of separation occurring between the plastron and plate.

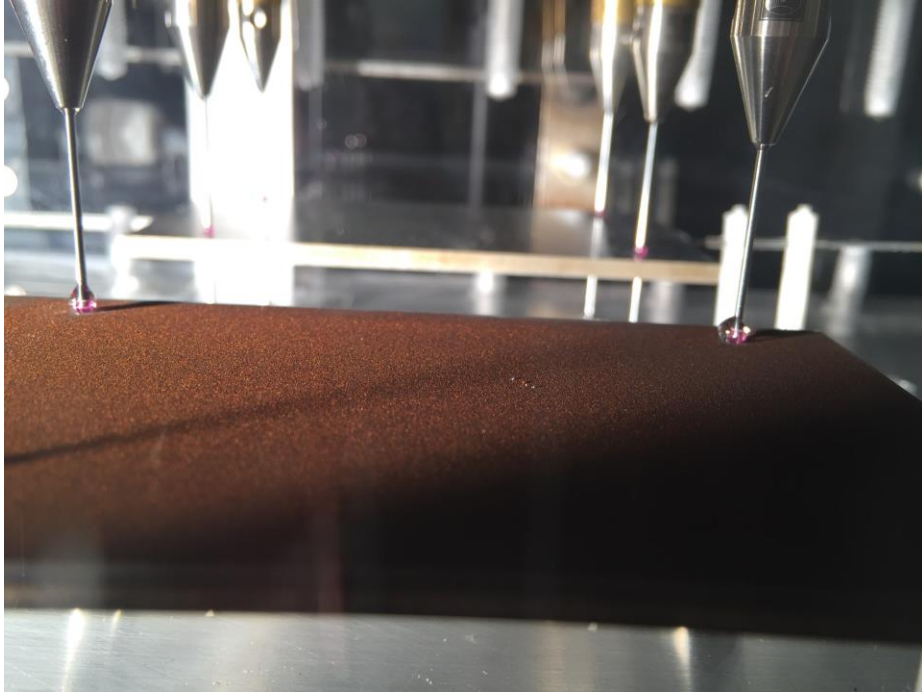


Figure 28. FLSP Plate Immediately After Channel Draining.

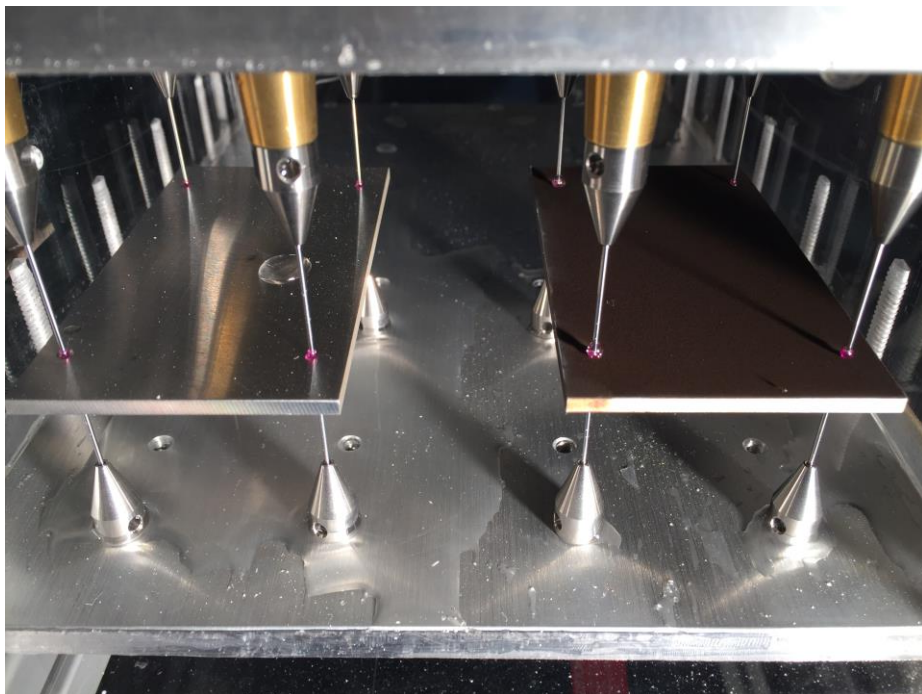


Figure 29. Plate Comparative Directly After Channel Draining.

Another interesting observation is how clean the FLSP plate is in comparison to the untreated plate. During the first test runs for observational purposes, the system still contained a small amount of scale contaminate from the tap water that was used in system leak tests. This scale was later removed through complete draining and cleaning of the system, but notice the presence of this scale, along with water droplets on the untreated plate, that are lacking on the FLSP plate. This supports the claims of a self-cleaning action inherent for superhydrophobic materials.

2. Plate Displacements

Although multiple testing runs were completed, the magnitudes and trends in the data were always identical; therefore, for brevity only one run will be presented here. For the testing run shown the FLSP plates displacement was being measured by sensor number 47173, and the base plate by sensor number 47174. The calibration data used to convert voltage to displacement for each sensor can be found in appendix 1.

As mentioned above for all test runs the pump was run at speeds of 0, 1100, 1500, 2000, 2500, 3000, and 3450 rpms. Table 2 lists the flow, velocity, channel Reynolds number, and plate Reynolds number for each testing speed.

Table 2. Parameters Associated with Pump Speed.

Speed (rpm)	0	1100	1500	2000	2500	3000	3450
Flow (m ³ /s)	0	0.0041	0.0058	0.0079	0.0101	0.0122	0.0143
Velocity (m/s)	0	0.1986	0.2811	0.3820	0.4890	0.5929	0.6906
Re Channel	0	26,780	37,904	51,500	65,920	79,928	93,112
Re Plate	0	20,085	28,428	38,625	49,440	59,946	69,834

The first recorded run was conducted with the pump off and the channel in a static condition. This is done to obtain a baseline voltage for each sensor. The average of this

data is then subtracted from each run in order to calculate the displacement from zero position. Figure 30 shows the voltage output from the sensors versus time.

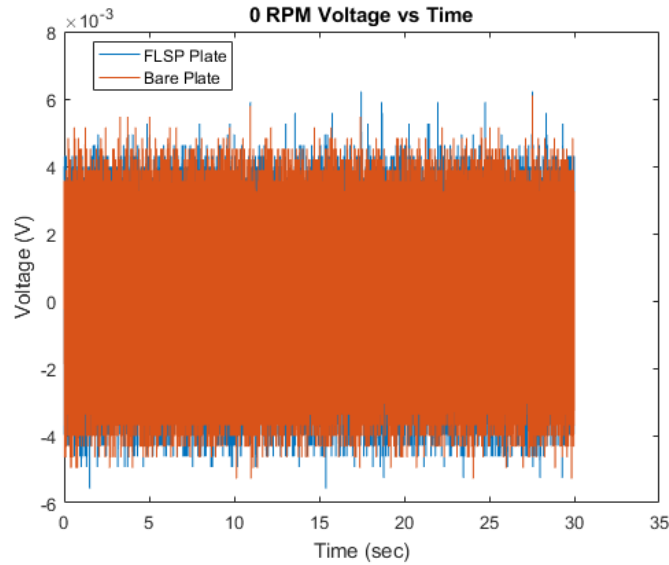


Figure 30. Sensor Voltage Output at 0 RPM.

As expected, in a static condition, the voltage output has been reduced to zero and therefore the plate displacements are zero. It has also been noted that each sensor produced a 3 kHz noise with a standard deviation of $0.74 \mu\text{m}$ when connected to the National Instruments equipment. While this produces a seemingly large ordinate band visually, it ultimately does not affect the data interpretation. Since the voltage is directly proportional to the sensor displacement through the seventh order polynomial fit calibration, sensor displacements versus time will henceforth be shown.

The next speed run shown in Figure 31, indicates a positive change in displacement for both plates, however the magnitude of displacement for the untreated plate is greater than that of the FLSP plate.

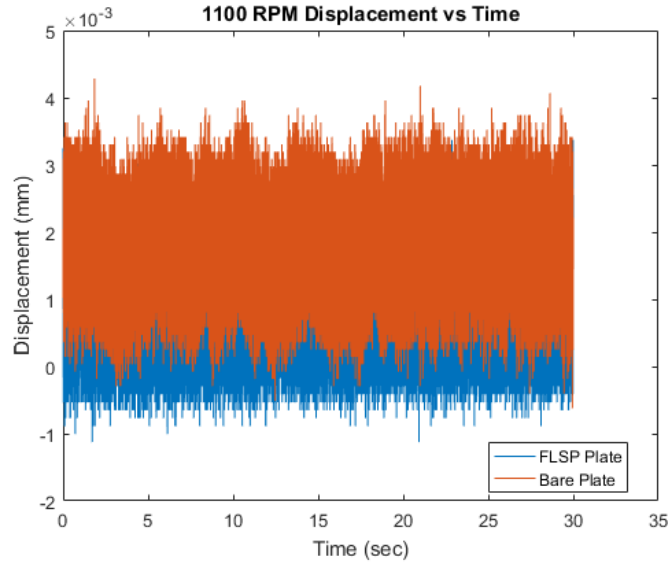


Figure 31. Displacement of Plates for 1100 RPM.

Here it becomes evident that the fluid interaction with the untreated plate is having a greater force imparted on it than that of the FLSP plate. In addition, the stability of position is greater for the FLSP plate than that of the untreated plate. At the 1500 rpm speed shown in Figure 32, the displacement increases as expected, along with the difference in displacement between the plates. The positional stability in the FLSP plate begins to degrade as the sensors time response begins to appear more like the untreated plates sensor output.

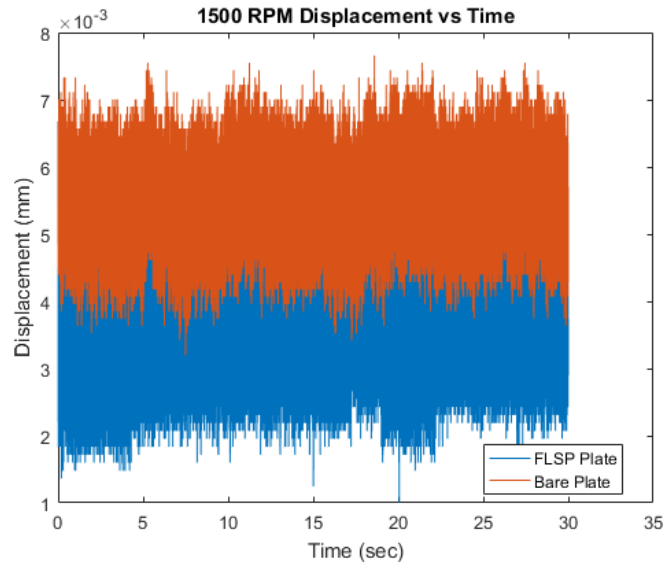


Figure 32. Displacement of Plates for 1500 RPM.

In the 2000 rpm run the positional stability of both plates are equal, but the magnitude of the difference between the displacements continues to increase as seen in Figure 33.

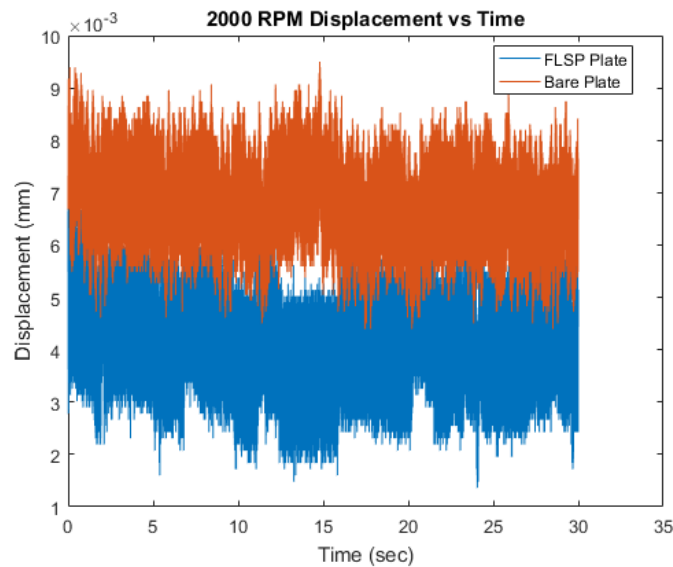


Figure 33. Displacement of Plates for 2000 RPM.

The next three speeds displayed in Figures 34, 35, and 36 continue to show both plates increasing in displacement as the velocity increases, however the difference in displacements between the plates begins to decrease. This is due to form drag increasing its dominance over film drag as the Reynolds increases.

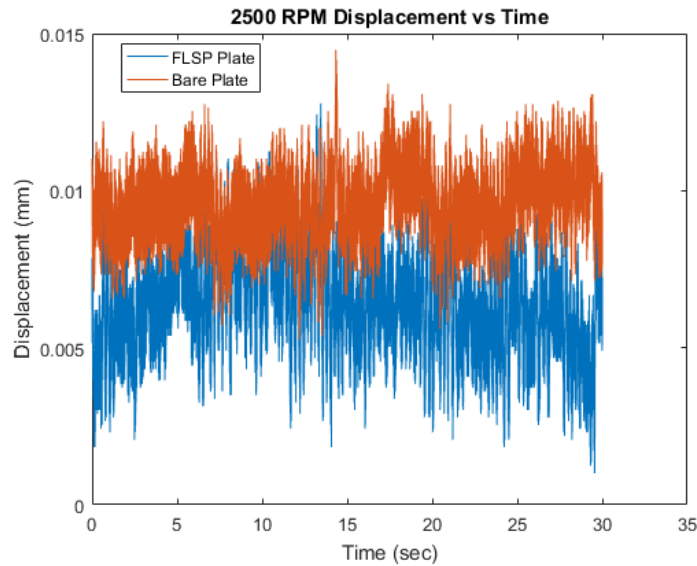


Figure 34. Displacement of Plates for 2500 RPM.

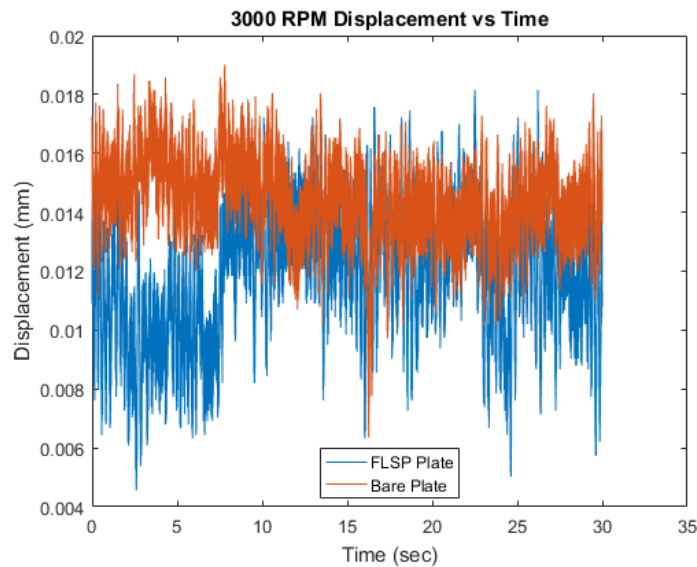


Figure 35. Displacement of Plates for 3000 RPM.

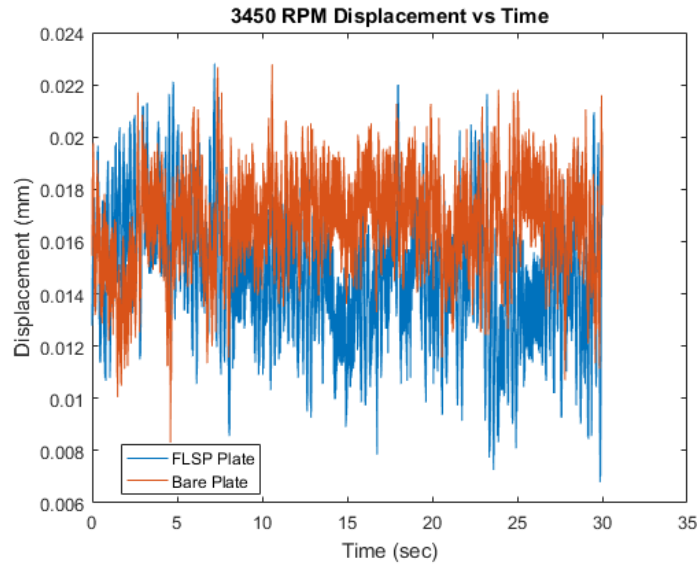


Figure 36. Displacement of Plates for 3450 RPM.

In the final speed run, the displacements of the two plates are nearly identical with an average difference of 0.002 mm. Figure 37 shows the difference in displacements between the plates as a function of Reynolds number.

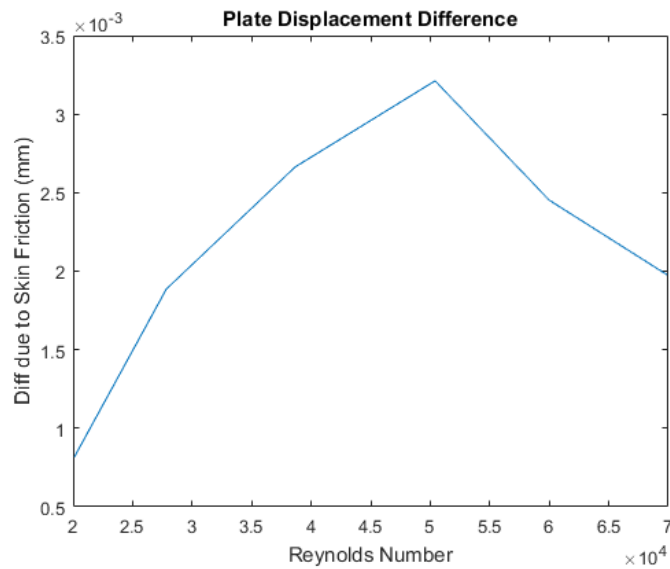


Figure 37. Difference in Displacement Between Test Plates.

After completing a series of speed runs, the channel was drained, and the specimen fixture was removed and placed on a bench for cantilever force calibration. In order to accurately determine the force necessary to displace the plates to a value that would actuate the cantilever in a manner seen by the DVRT sensors, a 0.0508 mm (0.002 in) polymer wire was looped around each plate. Then the wire was routed out the back of the specimen fixture and rotated 90 degrees around a low friction bearing to establish a tension line for hanging a mass. The height of the low friction bearing was adjusted to ensure the tension line was parallel with the fixture base. A 0.01 g plastic bag was attached to the end of the tension line and sand granules were added incrementally until a sensor displacement was achieved equal to that seen in the 3450 rpm runs. Table 3 shows the results for each sensor.

Table 3. Force and Sensor Displacement Values.

	0.01 g	0.8 g	1.9 g	3.3 g	4.2 g	5.1 g	5.57 g
Sensor 47173 (mm)	0	0.0024	0.0061	0.0105	0.0134	0.0163	0.0177
Sensor 47174 (mm)	0	0.0028	0.0064	0.0111	0.0141	0.0173	0.0188

The data in table 3 shows that the cantilever DVRT setup is indeed linear elastic and for the current preloading condition present, DVRT 47173 has a displacement constant of 3.08 N/mm while DVRT 47174 is 2.9 N/mm. When these displacement constants are applied to the data recorded from the channel runs, the total force applied to the plates can be calculated. Figure 38 shows the force exerted on each plate as a function of Reynolds number.

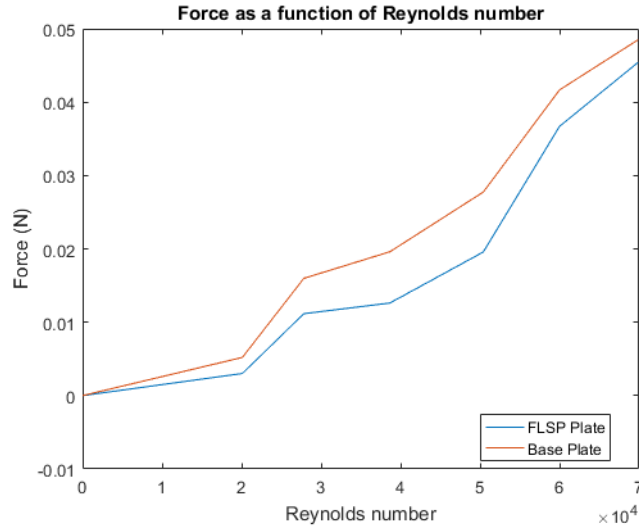


Figure 38. Force Exerted on Test Plates.

From here, it becomes quite clear there is a reduction in skin friction drag due to the presence of a FLSP functionalized surface, exhibiting superhydrophobic properties and inducing a plastron layer. This difference becomes most prevalent for this plate geometry between Reynolds numbers of 30,000 and 50,000. Beyond this range, form drags dominance overshadows any reduction in skin friction drag. Figure 39 and Table 4 summarize the reduction in skin friction drag as a function of Reynolds number.

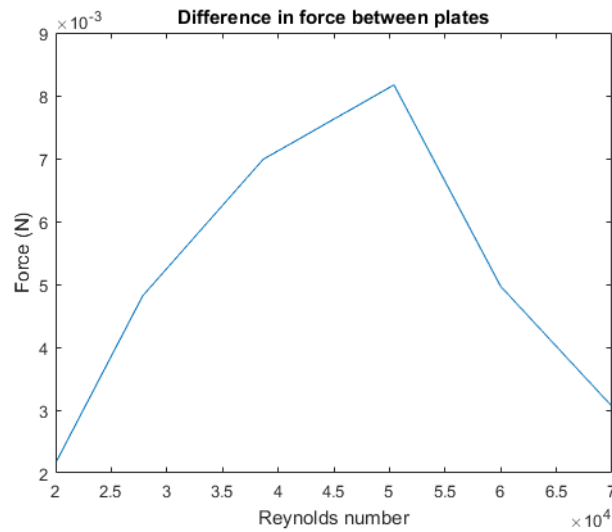


Figure 39. Reduction in Force due to Superhydrophobic Surface.

Table 4. Reduction in Skin Friction Force as a Result of Superhydrophobic Surface.

	Reynolds Number					
	20101	27832	38656	50407	59994	69890
Force (mN)	2.1916	4.8177	6.9875	8.1704	4.9668	3.0789

B. CORROSION TEST

Throughout the corrosion test, multiple samples of the same material and surface treatment were tested in parallel to ensure there were no anomalous findings. After completion of testing, all samples within a group behaved in a similar manner, therefore, for brevity only one sample from each group will be discussed here.

1. Visual Observations

After the first week of continuous contact with a salt fog atmosphere, each sample from the three groups appeared to be wet. This was an expected result for the superhydrophilic and untreated sample, but was more of a surprise for the superhydrophobic sample. The first hypothesis is that the atomized water vapor is small enough in scale to penetrate the micro scale surface features and bind to the metal substrate in areas of low density carbon. Figure 40 shows a superhydrophobic, superhydrophilic, and untreated sample directly after being removed from the fog chamber.

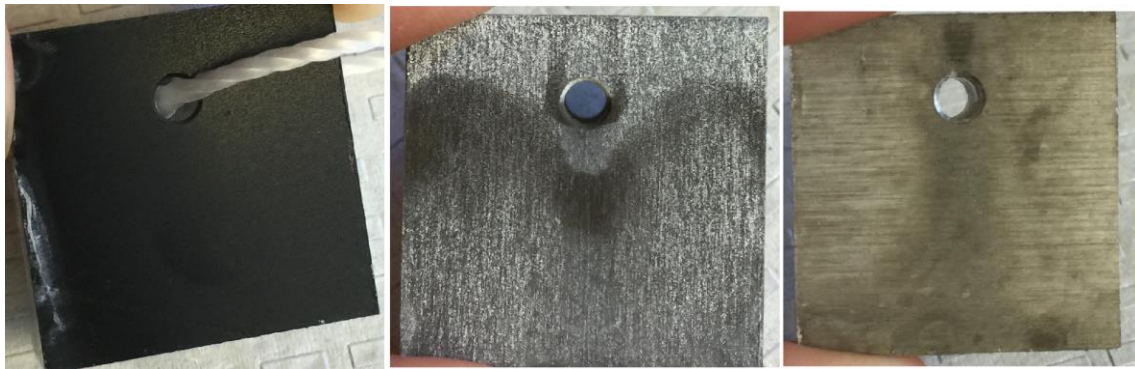


Figure 40. Corrosion Test Week 1, Left Superhydrophobic, Middle Superhydrophilic, Right Untreated.

It should be noted that while storing the superhydrophilic samples prior to testing, contact was made with zinc oxide, giving a whitish appearance on the surface. It was decided to include these samples in the testing since zinc oxide is more noble than aluminum, and the aluminum substrate will corrode preferentially to zinc oxide.

In week two, as illustrated in Figure 42 there is a significant accumulation of salt on the superhydrophobic sample, while the other two samples remain largely unchanged.



Figure 41. Corrosion Test Week 2, Left Superhydrophobic, Middle Superhydrophilic, Right Untreated.

Again, in week three there is visual evidence of salt accumulation and distribution on the superhydrophobic sample while the superhydrophilic and untreated samples remain mostly unchanged. While each sample pictured is of the same sample, opposite sides may be shown to illustrate an even presence of the findings seen for both sides of a sample. Figure 42 shows the samples after three weeks in the corrosion chamber.

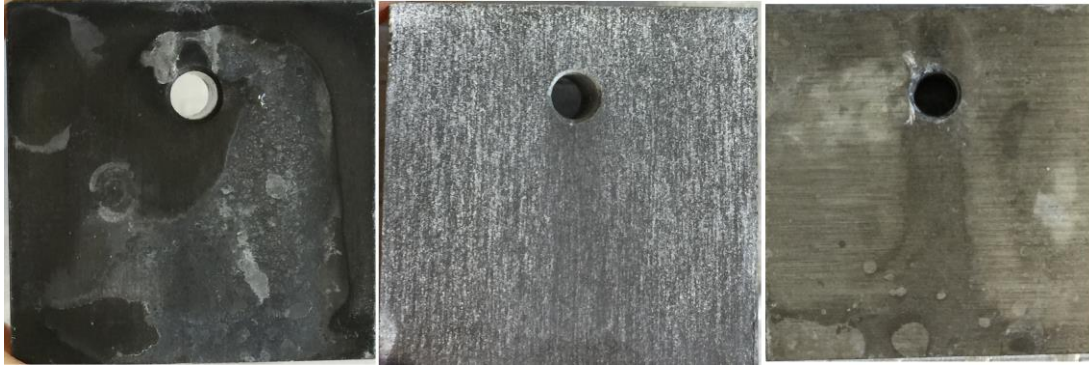


Figure 42. Corrosion Test Week 3, Left Superhydrophobic, Middle Superhydrophilic, Right Untreated.

In week four, significant changes and deviations begin to happen to the superhydrophobic sample compared to the other two. As seen in Figure 43, surface pitting begins to develop in areas of high salt concentration. These pits cause the removal of the functionalized surface leaving only the base material behind.



Figure 43. Corrosion Test Week 4, Left Superhydrophobic, Middle Superhydrophilic, Right Untreated.

When examined under a microscope (Figure 44) the evidence of salt accumulation and surface degradation on the superhydrophobic sample becomes quite clear. However, when examining the superhydrophilic sample, there is very little change, and almost no salt accumulation. The difference between superhydrophobic and superhydrophilic samples is quite vivid.

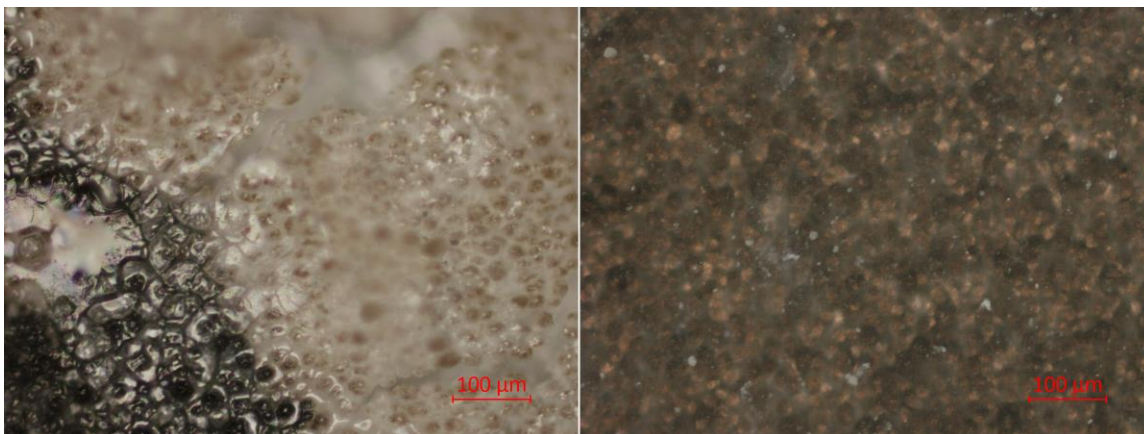


Figure 44. Corrosion Test Week 4 Magnified View, Left Superhydrophobic, Right Superhydrophilic.

Week 5 sees continued, rapid surface degradation of the superhydrophobic material, while again there is little change to the superhydrophilic material. Salt deposits begin to form on the untreated sample; however, there is no evidence of any pitting corrosion, as seen in Figure 45.

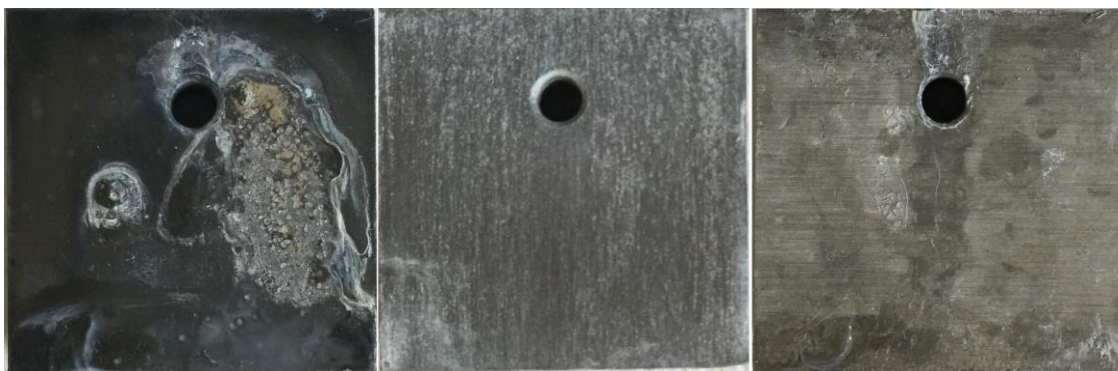


Figure 45. Corrosion Test Week 5, Left Superhydrophobic, Middle Superhydrophilic, Right Untreated.

The final week sees progressed salt accumulation on all three sample groups. There is pronounced crystal growth on the superhydrophobic sample as well as continued rapid degradation of the functionalized surface. The superhydrophilic sample begins to show crystal growth in the lower left corner along with some minor surface degradation. It should be noted that each sample has a thickness of 12.7 mm (0.5 in) that is untreated

bare metal. This surface on the bottom of the superhydrophilic sample was most likely the initiation point of the salt accumulation and not the functionalized surface itself. The untreated sample begins to show significant crystal growth, however, there is little evidence for pitting corrosion to have yet occurred. Figure 46 illustrates all these points.



Figure 46. Corrosion Test Week 6, Left Superhydrophobic, Middle Superhydrophilic, Right Untreated.

When examined under a microscope, the accelerated corrosion rate suffered by the superhydrophobic material becomes quite evident. In Figure 47, the superhydrophobic sample on the left shows a large pit of exposed bare metal. The blurred image in the foreground is a growth of salt crystals on the original surface level. In contrast, the superhydrophilic sample shows very little salt embedded into the micro structure of the surface. The untreated sample on the right is showing significant crystal growth on the surface, however, there is little signs of pitting. This would lead to the conclusion that functionalizing a surface with superhydrophobic properties would ultimately increase the corrosion rate of the surface, limiting the resiliency of the material.

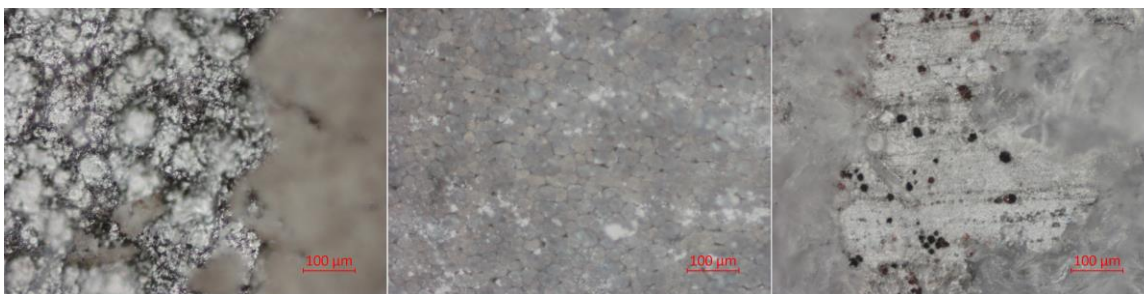


Figure 47. Corrosion Test Week 6 Magnified View, Left Superhydrophobic, Middle Superhydrophilic, Right Untreated.

2. Mass Measurements

Each week after visual observations, the mass of the samples was obtained following the removal of the non-wicking hanger and an appropriate amount of time for the samples to dry. Table 5 shows a summary of the results. The seventh week entry in the table are the mass measurements taken after the samples had been submersed in 95°C agitated deionized water for 30 minutes, and then allowed to dry for one week, to facilitate the removal of salt from the samples.

Table 5. Weekly Mass Measurements For Corrosion Samples.

Weeks / Samples	Superhydrophobic (g)	Superhydrophilic (g)	Untreated (g)
0	15.2467	15.4890	16.0658
1	15.2591	15.4979	16.0718
2	15.2665	15.4991	16.0770
3	15.2660	15.5008	16.0772
4	15.2733	15.5014	16.0830
5	15.2921	15.5013	16.1108
6	15.3123	15.5025	16.1180
7	15.2617	15.4938	16.0704

Figures 48-50 show the mass data plotted over time for graphical comparison.

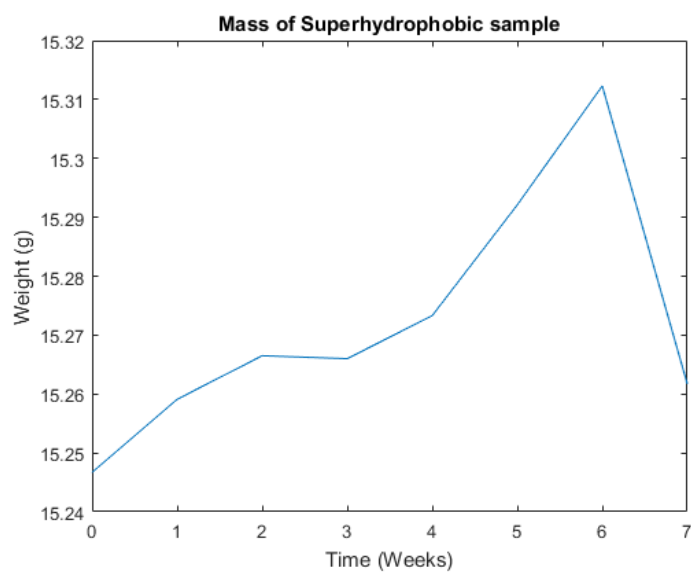


Figure 48. Superhydrophobic Sample Mass Over Time.

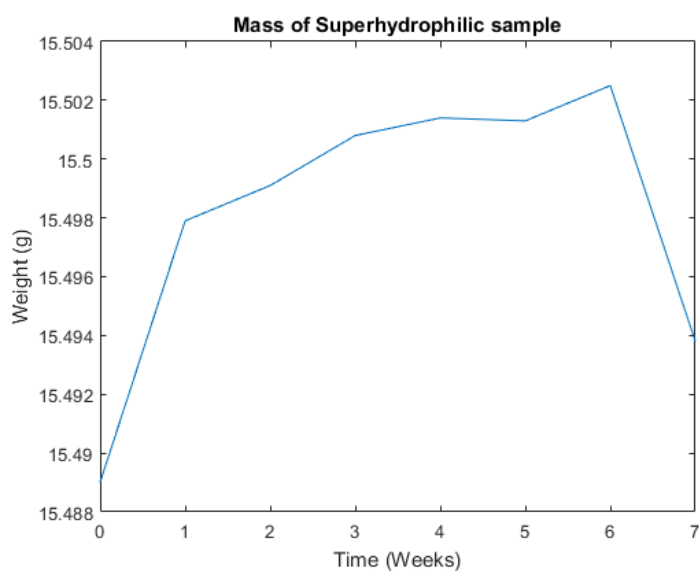


Figure 49. Superhydrophilic Sample Mass Over Time.

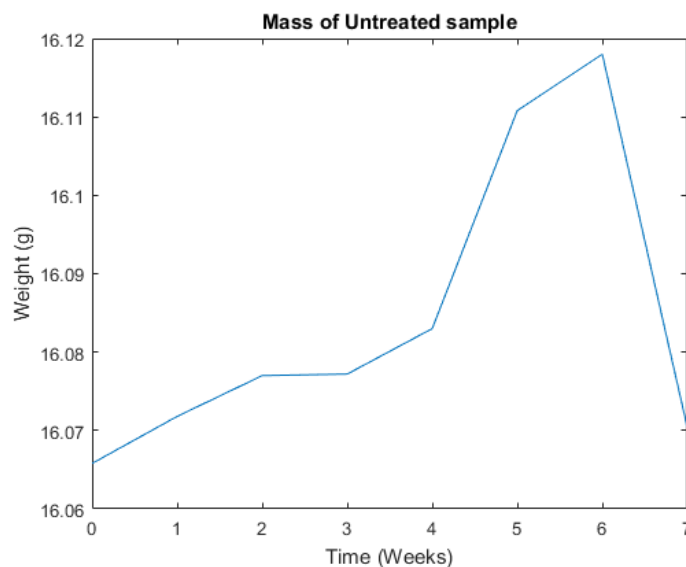


Figure 50. Untreated Sample Mass Over Time.

From the initiation of the test, each group of samples has an immediate gain in mass due to the deposition of salt, however the magnitude of that deposition is greatly varied. In the first two weeks, as evidenced by the visual observations, the superhydrophobic sample has the greatest mass gain of 0.0198 g while the superhydrophilic and untreated samples have mass gains of 0.0101 g and 0.0112 g respectively. After week two, until the conclusion of the test, the superhydrophilic samples mass gain tapers off to a moderate rate, only gaining an additional mass of 0.0034 g. In contrast, the rate of mass gain for both the superhydrophobic and untreated samples increased, gaining an additional 0.0458 g and 0.0410 g respectively.

Despite the similar mass gain rates of the superhydrophobic and untreated samples, as the visual observations would suggest, the superhydrophobic sample suffered greater corrosion rates than the other samples. This conclusion is supported when comparing the final mass measurement to the initial. It is expected that due to the conversion of aluminum to the heavier molecule, aluminum oxide, that mass would increase during corrosion. At the conclusion of the test, the superhydrophobic sample showed a total mass gain of 0.0150 g, the superhydrophilic sample was 0.0048 g, and the untreated sample was 0.0046 g. These numbers fully support the visual observations of

severe surface corrosion seen in the superhydrophobic sample, with only minor differences seen between the superhydrophilic and untreated samples, mainly the minor surface corrosion mentioned in Figure 46.

IV. CONCLUSIONS AND RECOMMENDATIONS

A. CONCLUSIONS

With the ability to extend superhydrophobic properties to metal surfaces through the use of femto-second laser surface processing, it is important to understand the possible commercial viability of such a material. To do this, an experiment was designed to analyze the hydrodynamic effects on drag due to FLSP treated surfaces along with the resiliency of the surfaces in harsh environmental conditions.

A flow channel was designed and constructed capable of analyzing two specimens in parallel to ensure equivalent flow conditions. An FLSP treated plate and an untreated plate were then placed in the channel. The system was run at various flow rates ranging from 227.12 l/min (60 gpm) to 832.79 l/min (220 gpm). The results of the fluid flow tests show a smaller momentum transfer to the FLSP treated plate as a result of a decrease in the skin friction coefficient of drag when compared to the untreated plate. This supports the theory of a partial slip condition existing due to the presence of a plastron layer from the superhydrophobic conditions. Therefore in commercial applications where skin friction drag is a high priority design consideration, the use of FLSP treatments may be warranted.

In addition to the hydrodynamic benefits, evidence of self-cleaning action due to superhydrophobic properties was also noted. Due to the rolling action of beaded water on the surface of the FLSP treated plate, dirt and debris was trapped in the water droplet and carried away from the surface of the plate.

In the final segment of this experiment, superhydrophobic, superhydrophilic, and untreated samples were subjected to an accelerated corrosion test to gauge the effect of surface processing on corrosion rates. Placed in an environment containing a 3.5% atomized salt solution held at 35°C for 1000 hours, the conditions of the sample surfaces and sample masses were monitored weekly. It became clear early that functionalizing a surface with superhydrophobic properties has a detrimental effect on corrosion resistance. The superhydrophobic sample exhibited an impressive salt retention capability over the

other two samples, as well as rapid surface degradation through pitting corrosion. At the conclusion of the test, the superhydrophobic sample showed the greatest mass gain, indicating a higher rate of corrosion when compared to the superhydrophilic and untreated samples.

While the hydrodynamic benefits of functionalizing a surface with superhydrophobic properties may be clear, the decrease in corrosion resistance may offset any practical benefits of the material.

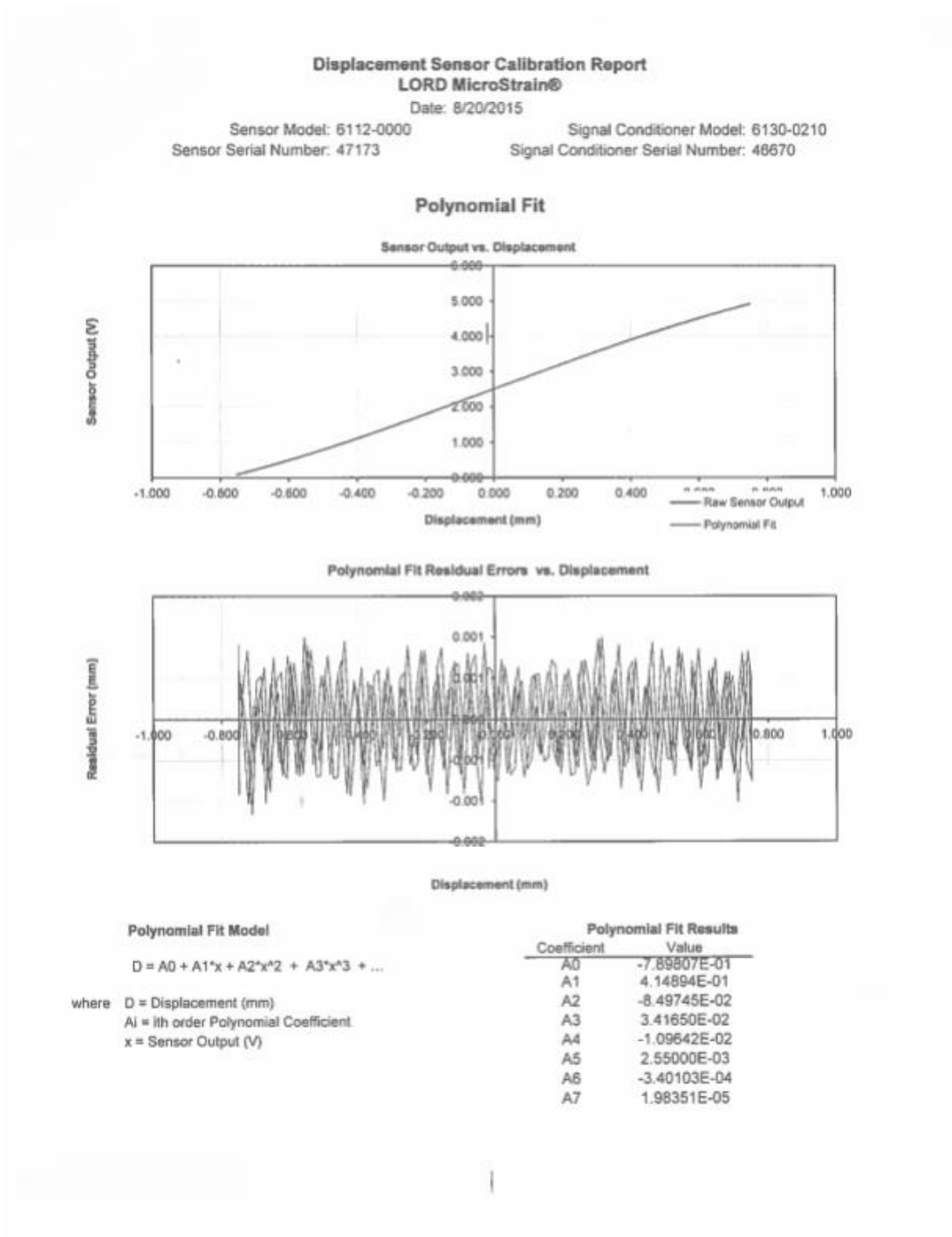
B. RECOMMENDATIONS

To better gage the practical applications of this material it is recommended that additional tests be run.

For analyzing the hydrodynamic benefits of superhydrophobic materials, the range of Reynolds numbers should be increased to include very low speed creeping flows as well as high speed flows. Particle image velocimetry should be implemented to study the velocity profile at the plastron water interface and quantify the slip velocity. Geometries other than a flat plate should be included, and lastly, inducing non uniform flow ahead of the channel's test section would be recommended to better understand the materials behavior in highly turbulent flows.

To better understand the effects on corrosion resistance, a wide range of processed materials should be included. This test was limited to the samples provided of aluminum 5083; however, other corrosive resistant materials such as titanium, stainless steels, brass, and copper should also be examined to determine if superhydrophobic functionalization is universally detrimental to corrosion rates, or isolated to aluminum alloys.

APPENDIX. SENSOR CALIBRATIONS



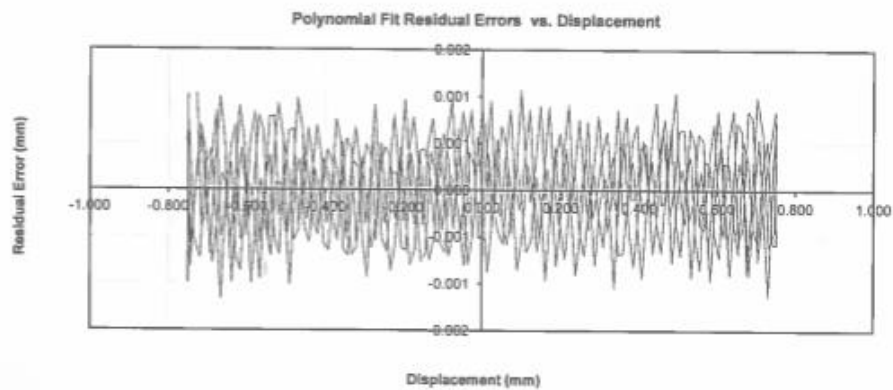
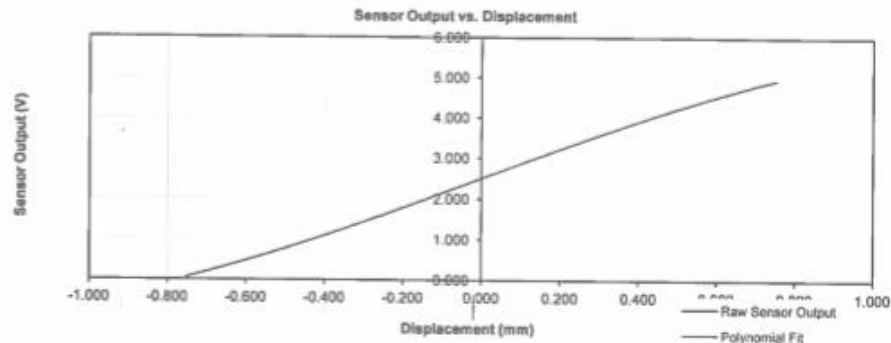
Displacement Sensor Calibration Report **LORD MicroStrain®**

Date: 8/20/2015

Sensor Model: 6112-0000
 Sensor Serial Number: 47174

Signal Conditioner Model: 6130-0210
 Signal Conditioner Serial Number: 46671

Polynomial Fit



Polynomial Fit Model

$$D = A_0 + A_1x + A_2x^2 + A_3x^3 + \dots$$

where D = Displacement (mm)

A_i = ith order Polynomial Coefficient

x = Sensor Output (V)

Polynomial Fit Results

Coefficient	Value
A0	-7.74279E-01
A1	3.95341E-01
A2	-6.88143E-02
A3	2.17524E-02
A4	-4.35740E-03
A5	5.36751E-04
A6	-3.00755E-05
A7	1.10362E-06

LIST OF REFERENCES

- [1] Operation and maintenance overview fiscal year 2017 budget estimates (2016) Comptroller.defense.gov. [Online]. Available: http://comptroller.defense.gov/Portals/45/Documents/defbudget/fy2017/fy2017_OM_Overview.pdf.
- [2] S. Wang and L. Jiang, Definition of superhydrophobic states, *Advanced Materials*, vol. 19, no. 21, pp. 3423–3424, 2007.
- [3] C. Neinhuis and W. Barthlott, Characterization and distribution of water-repellent, self-cleaning plant surfaces, *Annals of Botany*, vol. 79, no. 6, pp. 667–677, 1997.
- [4] B. Bhushan and Y. Jung, Micro- and nanoscale characterization of hydrophobic and hydrophilic leaf surfaces, *Nanotechnology*, vol. 17, no. 11, pp. 2758–2772, 2006.
- [5] L. Mahadevan and Y. Pomeau, Rolling droplets, *Physics of Fluids*, vol. 11, no. 9, pp. 2449–2453, 1999.
- [6] Y. Pal. (2016). *Production of super water-repellent products*. [Online]. Available: <http://contest.techbriefs.com/2016/entries/consumer-products/6951>
- [7] L. Wang, P. Nylen, A. Kjoniksen. (2016) *Icephobic surfaces and ice adhesion on thermal-spaying modified surfaces*. [Online]. Available: http://www.ir.hiof.no/~liw/lw_no2ice.htm
- [8] A. Cassie and S. Baxter, Wettability of porous surfaces, *Transactions of the Faraday Society*, vol. 40, p. 546, 1944.
- [9] G. Batchelor, *An Introduction to Fluid Dynamics*. Cambridge, UK: Cambridge Univ. Press, 2000.
- [10] Navier, C. L. M. H. *Mémoire sur les lois du mouvement des fluids* (Memory on the Laws of Fluid Motion). Paris, France; Mémoires de l'Académie Royale des Sciences de l'Institut de France 1823, pp. 389–440.
- [11] J. Rothstein, Slip on Superhydrophobic Surfaces, *Annu. Rev. Fluid Mech.*, vol. 42, no. 1, pp. 89–109, 2010.
- [12] E. Aljallis, M. Sarshar, R. Datla, V. Sikka, A. Jones and C. Choi, Experimental study of skin friction drag reduction on superhydrophobic flat plates in high Reynolds number boundary layer flow, *Physics of Fluids*, vol. 25, no. 2, p. 025103, 2013.

- [13] T. Min and J. Kim, Effects of hydrophobic surfaces on skin-friction drag, *Physics of Fluids* vol. 16, p. L55–L58, 2004.
- [14] T. Min and J. Kim, Effects of hydrophobic surface on stability and transition, *Physics of Fluids* vol. 17, p. 108106, 2005.
- [15] M. B. Martell, J. B. Perot, and J. P. Rothstein, Direct numerical simulations of turbulent flows over superhydrophobic surfaces, *J. Fluid Mech.* Vol. 620, p. 31–41, 2009.
- [16] M. B. Martell, J. P Rothstein, and J. B. Perot, An analysis of superhydrophobic turbulent drag reduction mechanisms using direct numerical simulation, *Physics of Fluids* vol. 22, p. 065102, 2010.
- [17] C. Cottin-Bizonne, B. Cross, A. Steinberger and E. Charlaix, Boundary Slip on Smooth Hydrophobic Surfaces: Intrinsic Effects and Possible Artifacts, *Physical Review Letters*, vol. 94, no. 5, 2005.
- [18] D. Maynes, K. Jeffs, B. Woolford and B. Webb, Laminar flow in a microchannel with hydrophobic surface patterned microribs oriented parallel to the flow direction, *Physics of Fluids*, vol. 19, no. 9, p. 093603, 2007.
- [19] J. Ou and J. Rothstein, Direct velocity measurements of the flow past drag-reducing ultrahydrophobic surfaces, *Physics of Fluids*, vol. 17, no. 10, p. 103606, 2005.
- [20] K. Fukuda, J. Tokunaga, T. Nobunaga, T. Nakatani, T. Iwasaki and Y. Kunitake, Frictional drag reduction with air lubricant over a super-water-repellent surface, *Journal of Marine Science and Technology*, vol. 5, no. 3, pp. 123–130, 2000.
- [21] B. Elbing, E. Winkel, K. Lay, S. Ceccio, D. Dowling and M. Perlin, Bubble-induced skin-friction drag reduction and the abrupt transition to air-layer drag reduction, *Journal of Fluid Mechanics*, vol. 612, 2008.
- [22] W. Chen, A. Fadeev, M. Hsieh, D. Öner, J. Youngblood and T. McCarthy, Ultrahydrophobic and Ultralyophobic Surfaces: Some Comments and Examples, *Langmuir*, vol. 15, no. 10, pp. 3395–3399, 1999.
- [23] C. Henoch et al, Turbulent drag reduction using superhydrophobic surfaces, Collection of Technical Papers: *Third AIAA Flow Control Conference*, 2006, Vol. 2, p.840.
- [24] R. Daniello, N. Waterhouse and J. Rothstein, Drag reduction in turbulent flows over superhydrophobic surfaces, *Physics of Fluids*, vol. 21, no. 8, p. 085103, 2009.

- [25] E. Aljallis, M. Sarshar, R. Datla, V. Sikka, A. Jones and C. Choi, Experimental study of skin friction drag reduction on superhydrophobic flat plates in high Reynolds number boundary layer flow, *Physics of Fluids*, vol. 25, no. 2, p. 025103, 2013.
- [26] A. Kietzig, S. Hatzikiriakos and P. Englezos, Patterned Superhydrophobic Metallic Surfaces, *Langmuir*, vol. 25, no. 8, pp. 4821–4827, 2009.
- [27] C. Zuhlke, T. Anderson, P. Li, M. Lucis, N. Roth, J. Shield, B. Terry and D. Alexander, Superhydrophobic metallic surfaces functionalized via femtosecond laser surface processing for long term air film retention when submerged in liquid, *Laser-based Micro- and Nanoprocessing IX*, 2015.
- [28] Introduction (2016) [www.uio.no](http://www.uio.no/studier/emner/matnat/math/MEK4450/h11/undervisningsmateriale/modul-5/Pipeflow_intro.pdf). [Online]. Available: https://www.uio.no/studier/emner/matnat/math/MEK4450/h11/undervisningsmateriale/modul-5/Pipeflow_intro.pdf.
- [29] Microminiature Gauging DVRT® | LORD Sensing Systems (2016) [Microstrain.com](http://www.microstrain.com/displacement/mg-dvrt). [Online]. Available: <http://www.microstrain.com/displacement/mg-dvrt>. [Accessed: 15- Nov- 2016].
- [30] A. Trim, H. Braaten, H. Lie and M. Tognarelli, Experimental investigation of vortex-induced vibration of long marine risers, *J. Fluid Structures*, vol. 21 no.3, p. 335361, 2016.

THIS PAGE INTENTIONALLY LEFT BLANK

INITIAL DISTRIBUTION LIST

1. Defense Technical Information Center
Ft. Belvoir, Virginia
2. Dudley Knox Library
Naval Postgraduate School
Monterey, California